AD-A265 698

NTATION PAGE

Form Approved
OMB No. 0704-0188

1 AGENCY USE ONLY (Leave blank)	2 REPORT DATE	3 REPORT TYPE AND DATES COVERED
	March 1993	Professional paper

4 TITLE AND SUBTITLE
NONLINEAR FINITE ELEMENT ANALYSIS OF COMPOSITE FLEXTENSIONAL TRANSDUCER SHELL

5 FUNDING NUMBERS
PR: SV70
PE: 0204311N
WU: DN302195

6 AUTHOR(S)
R. C. Shaw

7 PERFORMING ORGANIZATION NAME(S) AND ADDRESS(ES)
Naval Command, Control and Ocean Surveillance Center (NCCOSC)
RDT&E Division
San Diego, CA 92152-5001

8 PERFORMING ORGANIZATION REPORT NUMBER

9 SPONSORING/MONITORING AGENCY NAME(S) AND ADDRESS(ES)
Naval Command, Control and Ocean Surveillance Center (NCCOSC)
RDT&E Division
San Diego, CA 92152-5001

10 SPONSORING/MONITORING AGENCY REPORT NUMBER

11 SUPPLEMENTARY NOTES

12a DISTRIBUTION/AVAILABILITY STATEMENT
Approved for public release; distribution is unlimited.

12b DISTRIBUTION CODE

13 ABSTRACT (Maximum 200 words)

Presented here is the result of a Finite Element Analysis (FEA) and its correlation with test data for a Class IV flextensional underwater acoustic transducer. The thick, elliptical fiberglass/epoxy shell of the transducer Finite Element Model (FEM) was modeled with 20-node solid elements using effective engineering properties derived from a micromechanics theory. Unidirectional gap elements were used to model the clearance between the end curves of the shell and the two D-shaped aluminum inserts. The D-inserts were placed along the major axis of the shell to transmit the driving power of the piezoelectic ceramic stack in order to excite shell's flaxural modes for an efficient acoustic radiation. The model also featured large deformation. The predicted global displacements of the shell, as well as the local strain values at several critical locations in the shell, correlated very well with the test data obtained from the stack preload and hydrostatic pressure tests. Gapping between the end curve of the shell and the D-insert, which was detected during the pressure test, was also predicted in the analysis. Gapping has been shown to be detrimental to the structural, as well as the acoustic performance of the shell.

The success of this pilot model, in accurately predicting the structural behavior of the transducer shell under simulated loading conditions, has lead to a series of FEA studies to determine the sensitivities of the shell's structural performance to thickness variation and to nonuniform material property distribution in the shell. Nonuniform material property distribution arise from the variation in parameters, such as moduli of the constituents, fiber volume fraction, and ply arrangement of the laminates. The model is currently being used to investigate the concept of flexible D-insert designs conforming to the deformed shape of the shell in order to maintain a closed shell-to-D-insert contact for deeper underwater applications.

Published in *Proceedings* of the 21st Annual International Meeting of Subgroup GTp-9, November 1992.

14 SUBJECT TERMS
active surveillance (reverberation)
data processing
passive acoustic surveillance

15 NUMBER OF PAGES

16 PRICE CODE

17 SECURITY CLASSIFICATION OF REPORT	18 SECURITY CLASSIFICATION OF THIS PAGE	19 SECURITY CLASSIFICATION OF ABSTRACT	20 LIMITATION OF ABSTRACT
UNCLASSIFIED	UNCLASSIFIED	UNCLASSIFIED	SAME AS REPORT

21a NAME OF RESPONSIBLE INDIVIDUAL	21b TELEPHONE (Include Area Code)	21c OFFICE SYMBOL
R. C. Shaw	(619) 553-3230	Code 933

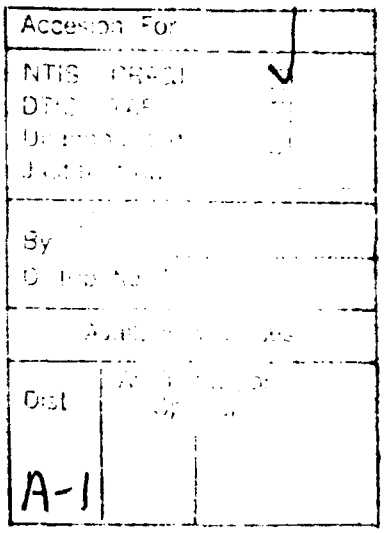

NONLINEAR FINITE ELEMENT ANALYSIS OF COMPOSITE FLEXTENSIONAL TRANSDUCER SHELL

R. C. SHAW

NAVAL COMMAND, CONTROL AND OCEAN SURVEILLANCE CENTER
SAN DIEGO, CALIFORNIA

ABSTRACT

Presented here is the result of a Finite Element Analysis (FEA) and its correlation with test data for a Class IV flextensional underwater acoustic transducer. The thick, elliptical fiberglass/epoxy shell of the transducer Finite Element Model (FEM) was modeled with 20-node solid elements using effective engineering properties derived from a micromechanics theory. Unidirectional gap elements were used to model the clearance between the end curves of the shell and the two D-shaped aluminum inserts. The D-inserts were placed along the major axis of the shell to transmit the driving power of the piezoelectric ceramic stack in order to excite shell's flexural modes for an efficient acoustic radiation. The model also featured large deformation. The predicted global displacements of the shell, as well as the local strain values at several critical locations in the shell, correlated very well with the test data obtained from the stack preload and hydrostatic pressure tests. Gapping between the end curve of the shell and the D-insert, which was detected during the pressure test, was also predicted in the analysis. Gapping has been shown to be detrimental to the structural, as well as the acoustic performance of the shell.

The success of this pilot model, in accurately predicting the structural behavior of the transducer shell under simulated loading conditions, has lead to a series of FEA studies to determine the sensitivities of the shell's structural performance to thickness variation and to nonuniform material property distribution in the shell. Nonuniform material property distribution arises from the variation in parameters, such as moduli of the constituents, fiber volume fraction, and ply arrangement of the laminates. The model is currently being used to investigate the concept of flexible D-insert designs conforming to the deformed shape of the shell in order to maintain a closed shell-to-D-insert contact for deeper underwater applications.

INTRODUCTION

For the past few years, the Research, Development, Test and Evaluation Division of Naval Command, Control and Ocean Surveillance Center (NRaD), has been tasked to develop a high-power, low-frequency transducer as an effective underwater sound source. A 2-inch thick fiberglass/epoxy shell with elliptical cross section has been developed recently for the projector element of the Class IV flextensional design. In developing this transducer to achieve adequate strength in the shell and durability in service, it is imperative to test the strength of the composite shell under simulated loading conditions. In light of the complicated process of manufacturing composite shells, it is virtually impossible to bring important parameters such as shell thickness and the material strength distribution within the shell to typically allowable tolerances for the metallic parts. Due to the random nature of these variations and high cost of manufacturing the composite shells, it is impractical to produce enough specimens for strength tests across the full spectrum of these variables. Therefore, an analytical approach is necessary to complement a few control tests.

In many FEA programs that can analyze the composite structures, the Classical Lamination Theory (CLT) is used to "smear" the ply material properties of composites so that the FEA program sees a homogeneous body with equivalent orthotropic properties. Programs that use CLT can calculate ply-by-ply results, but they cannot take into account through-thickness effects (in-plane

normal and interlaminar shear stresses). MSC/NASTRAN (1989) developed a single plate or shell element with through-thickness shear effect by incorporating the equilibrium conditions of a "bent beam". However, this shell element is suitable for thin shell application, but not for the thick shell such as the Class IV flextensional shell. A study on limitations and shortcomings of using MSC/NASTRAN's composite shell elements for analysis of thick shells was reported by Shaw (1989). Using three-dimensional (3-D) solid elements is an alternative to model the composite structure. Rouse (1988) pointed out that 3-D solid elements coupled with lamination theory to model laminated structures has become more popular among the composite designers. The use of "smeared" material properties for the solid elements means fewer elements are needed to model the structure, but ply data are still available at the end of analysis. This approach is chosen here to analyze flextensional transducer shells. The ABAQUS FEA program is executed on a Convex mini-supercomputer. The analysis results are validated through comparisons with test data obtained from stack preload and hydrostatic pressure tests. The data compared include the major and minor axis deflections and strain values at several critical locations in the shell. The natural frequencies predicted by the model are also compared with the frequency data obtained from the modal survey on the bare shell.

FINITE ELEMENT ANALYSIS OF COMPOSITE SHELL

MODEL GEOMETRY

Two 5.7-inch long, 2-inch thick (nominal) fiberglass/epoxy shells were fabricated for the tests. The test configuration for the test specimen (Shell 010) showing strain gage locations is giving in Figure 1. In constructing the FEM of the composite shell, the inner surface of the shell, which consists of two radii (at "flat" and "curve") meeting at a transition point, was chosen as the reference surface on which the geometry of the model was defined. Two cylindrical coordinate systems originated at the centers of the "flat" and "curve" were used to facilitate the generation of the shell model using the PATRAN FEM pre and postprocessors hosted on a MicroVAX II/GPX workstation. Figure 2 shows a 1/8-symmetric (1-quadrant and 1/2-length), 3-D FEM of the test specimen constructed with ABAQUS' 20-node solid elements with 2x2x2 reduced integration points (C3D20R). The shell is interfaced at the inner curve by a 4-inch long, D-shaped aluminum insert which was also modeled with C3D20R solid elements. The D-insert has a matching radius slightly smaller than the end radius of the shell. Thus, a clearance exists along the D-insert and shell interface, as shown in Figure 3. This initial clearance was modeled with ABAQUS unidirectional gap elements (GAPUNI) defined by a set of matching pairs of D-insert and shell nodes along the radial direction of the D-insert. The presence of these gap elements, which close and transmit compressive forces in the radial direction of the D-insert when loaded, makes the shell model a FEM with the "boundary nonlinearity". Note that current analyses also consider the "geometric nonlinearity" to account for the possible large deformations in the loaded shell.

"SMEARED" MATERIAL PROPERTIES

The laminated construction of the shell wall in the current Class IV transducer design can be considered as a balanced, symmetric, angle-ply laminate (i.e., there are equal numbers of plies with an equal but opposite orientation angle of 7^{C}). Instead of performing a time-consuming, ply-by-ply material and structural definition for the composite, the effective engineering properties of the laminate were estimated from the referenced micromechanical equations. These equations, expressing the ply properties in terms of their constituent properties and volume fractions, are (1) the rule of mixtures (see Halpin, 1984) to estimate the longitudinal modulus (E_{11}) and Poisson's ratio (v_{12}), and (2) the Halpin-Tsai empirical formulas (see Halpin, 1984) to approximate the transverse and in-plane shear moduli (E_{22} and G_{12} respectively). To account for the variation in the fiber volume fraction through the thickness, the values of "smeared" orthotropic material properties for the test specimen were evaluated for a range of fiber volume fractions between 55 and 65 percent. Best estimates of the upper- and lower-bound values based on results of that

evaluation were provided by Maltby (1988) and are tabulated in Table 1. The material orthotropy was accounted for by orienting the material properties of the elements in the "flat" and "curve" portions of the shell to the respective local cylindrical coordinate system defined for the model, as shown in the figure below Table 1. However, only linear and homogeneous properties were used in the analyses.

BOUNDARY AND LOADING CONDITIONS

The symmetry conditions in X-Y, Y-Z and Z-X planes shown in Figure 2 provide adequate constraints on the model in the modal analysis to calculate natural frequencies of the shell and in the stress analysis to predict the response of the shell due to the stack preload and the hydrostatic pressure. Before pressure is applied in the hydrostatic pressure test, the shell is preloaded in the stack to 136 kips. To simulate this loading condition, the analysis is performed in two steps. In step 1, a prescribed displacement in the outward direction of the major axis (X-direction) is imposed on the wedge end of the extension rod (node 2073 in Figure 2) such that the reacting force in the rod, which replaces the ceramic stack in the test configuration and is modeled as a spring element with a stiffness equivalent to that of the extension bar and the wedge assemly in series ($K = 2.1438 \times 10^6$ lb/in), reaches the value of 136 kips. Note that a constraint equation in X-direction is imposed among the nodes at the slot of the D-insert (nodes 1639, 1647, 1655, 1900, 1963, 2026, etc.) to ensure that the constraint force induced at node 2073 due to the precribed displacement is properly transmitted to the D-insert. Also note that several iterations are necessary to reach the desirable value of the preload in step 1. In step 2, the pressure is applied at the external surface of the shell while this prescribed displacment is maintained, even though the curve end of the shell deflects outward under increasing pressure. This results in a relaxation of the stack load.

Table 1. Estimated Engineering Properties for Shell 010

	"Smeared" Engineering Properties ($\times 10^6$ psi)						Poisson's Ratios
	E_{11}	E_{22}	E_{33}	G_{12}	G_{13}	G_{23}	$\nu_{12}, \nu_{13}, \nu_{23}$
Lower-Bound	5.7	1.8	1.2	0.57	0.57	0.57	0.3
Upper-Bound	7.0	2.4	2.3	0.90	0.90	0.90	0.3

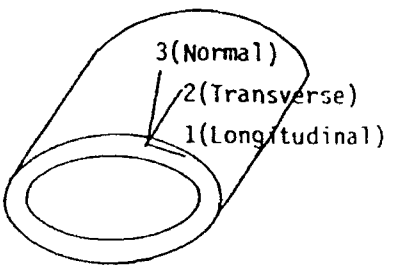

Coordinate Systems For Engineering Properties

Notes: (1) The engineering constants defined above are transformed into R (radial), Θ(circumferential), and Z (axial) coordinate system used in ABAQUS analyses. The indices 1, 2, and 3 in Table 1 become 2, 3, and 1 in ABAQUS.

(2) The conditions relating Poisson's ratios to Young's moduli, $\nu_{ij}/E_{ii} = \nu_{ji}/E_{jj}$ (i, j = 1, 2, and 3), apply when reversing indices of ν_{ij}.

ANALYSIS RESULTS AND COMPARISON WITH TEST DATA

MODAL ANALYSIS

The calculated natural frequencies of the two models encompass the test result obtained from a modal survey of the bare shell, with the lower-bound property model rendering better correlation. The comparisons are given in Table 2. The lower-bound property model predicts the lowest natural frequency to be at 164.41 Hz, which is within 3.9 percent of the test result of 171 Hz obtained in a modal survey by Maltby (1991). The upper-bound property model overpredicts the lowest natural frequency by 8.4 percent at 185.33 Hz. The predicted mode shapes for the first two modes are shown in Figures 4a and 4b. No mode shape data from the modal survey was available for comparison.

Table 2. Dynamic Characteristics of Shell 010,
Modal Analysis Versus Modal Survey Data

	Natural Frequencies (Hz)			
	1st Mode		2nd Mode	3rd Mode
	Hz	Test Comp	Hz	Hz
Lower-Bound Model	164.41	-3.9%	840.50	1,757.6
Upper-Bound Model	185.33	+8.4%	960.29	1,950.5
Modal Survey Data	171.	--		

As shown in Figure 4a, the opposite-phased bending of the "flat" and the "curve" characterizes the lowest mode of free vibration for the oval shell, i.e., the "flat" bends inward and the "curve" displaces outward. Although the concept for flextensional transducers is based on the mutual coupling between two perpendicular, flexural modes of vibration for an oval shell, the interaction between the membrane and the flexural modes plays an important role in determining the structural behaviors of the shell.

STACK PRELOAD TEST RESULTS

The prescribed displacements at node 2073 to induce a 136-kip stack preload in the first load step are 0.2654 inch and 0.2330 inch for the lower- and upper-bound property models respectively. The stack loads are plotted against the major and minor axis displacements and the results are compared with the test data, as shown in Figures 5a and 5b. As can be seen, excellent correlations are achieved, as the test results fall between the predicted values of the two models.

HYDROSTATIC PRESSURE TEST RESULTS

The prescribed displacement derived in the first load step is maintained when external pressure is applied in the second load step. The flattening of the shell under external pressure relaxes the stack load in the D-insert. The calculated results of pressure load versus stack load are plotted against test data and shown in Figure 6. Fairly good correlation between the calculated and test results is seen. Note that each calculated data point in Figure 6 represents a convergent solution of the incremental loading procedure carried out in ABAQUS. A total pressure of 459.1 psi and four increments are specified at the beginning of the second load step in the analysis. As planned, convergent solutions are obtained in four equal increments for the upper-bound model. However, after convergent solutions are obtained at the first two equal increments for the lower-bound property model, the size of the pressure increment was reduced by one-half automatically to reach

a solution at a higher pressure level in ABAQUS computer run. In all, six load increments are necessary to reach a solution for 459.1-psi pressure. As shown in Figure 6, an almost identical linear pressure-to-stack load relationship exists for the lower- and upper-bound property models, up to three-fourth of the way (344.3 psi) of the maximum pressure. But the relationships become nonlinear and diverge for the two models when pressurized beyond 344.3 psi. This observation indicates that some kind of nonlinear behavior, other than the nonlinear material behavior, must have happened during the last increment of pressure loading that changed the load paths and caused load redistribution in the shell models. This question will be answered later.

The minor axis displacement versus pressure load curve is plotted in Figure 7. It seems that the analysis models underestimate the flexural stiffness of the shell. The minor axis deflection for the upper-bound property model is 0.289 inch at the maximum pressure of 459.1 psi, as compared to 0.176 inch for the test, a 64 percent discrepancy. Three important observations are made regarding results shown in Figure 7:

1. The unloading curve does not follow the loading curve for the test. This indicates that some nonlinear material response has taken place during the pressure test. It should be noted that the unloading curve obtained in the analytical simulation of unloading follows the loading curve almost exactly. This result is not surprising since linear-elastic material properties were used in both analysis models.

2. The pressure load and displacement relationship becomes nonlinear when the shell is pressurized beyond 344.3 psi. This nonlinear behavior is the result of permitting large deformations in the current analysis.

3. The flexural behavior is sensitive to the variations of the material properties, especially when the shell is subjected to high pressure.

GAPPING OF SHELL

A closer look at the progression of deformation resulting from incremental loading of pressure reveals that gapping has occurred at the shell and D-insert interface at the last load increment. The shell and D-insert interface remains closed during the first three increments of pressure loading (up to 344.3 psi), but opens and forms a gap near the end of the shell when the external pressure reaches 459.1 psi, as shown in Figure 8. An enlarged view clearly depicting this interface gapping is giving in Figure 9. It is important to report that this behavior was also observed in the pressure test. Gapping can be attributable to an interface condition that develops between the shell and the D-insert. As pressure load increases and flattens the shell, the end curve of the shell takes on a parabolic shape and its radius of curvature eventually becomes smaller than the D-insert and separation occurs at the apex of the curve. This observation signals the presence of large deformation at the curve of shell. Gapping starts from the apex of the end curve and propagates upward along the interface and would, eventually, cause the shell to pivot about the upper edge of the D-insert if higher pressure is applied. This phenomenon is undesirable for three reasons as follows:

1. The concept of a flextensional transducer relies on the premise that a close coupling exists between the ceramic stack length mode and shell flexural modes. In the most general sense, the stack extends, transmitting its load through the D-inserts to the shell, which in turn flexes, thus driving the name flextensional. The movement of the contact area away from the apex of the shell moves the path of the stack load away from the major axis of the shell and reduces the effectiveness of the D-insert in transmitting the maximum load from the stack to the shell. The reduction of load tramsmitted by the D-insert undoubtly decreases the bending moment generated to drive the flexural modes of the shell vigorously and, therefore, can reduce the acoustic performance of the shell.

2. Gapping causes redistribution of contact load along the interface to a less favorable position. The contact stresses are more concentrated on the area of shell that maintains contact with the upper edge of D-insert. The significant stress components for the last load increment of the upper-bound property model are given in Figures 10 to 13. The stress component most affected by the change of interface conditon is the radial stress (S_{33}). As shown in Figure 10, the gradients of this stress distribution becomes more abrupt when the interface condition changes. The maximum radial stress is 10,147 psi in compression, which occurs at the narrow strip of shell's inner surface area that remains in contact with D-insert. However, the areas immediately surrounding the contact are in tension (up to 2,386 psi) due to the discontinuity of contact. Although the magnitude of this through-thickness normal tensile stress is not very high, it is detrimental considering the long fatigue life demanded of the shell.

3. The oval shell, which is supported firmly at its curve ends by the D-inserts, is tuned to vibrate at a certain frequency band during the operation of a transducer. But, gapping between the shell and the D-insert caused by high depth pressures alters the end-support condition of the shell. As shown in Figure 9, the gap widens and the shell is supported by approximately the upper one-fifth of the D-insert when the pressure reaches 459.1 psi. The reduction of the end-supporting area for the shell changes the dynamic characteristics of the shell and, therefore, affects the resonance condition of the shell during operation of the transducer at greater depths.

HOOP AND SHEAR STRESS DISTRIBUTIONS

Other significant stress components whose distributions are not affected much by the presence of the gap are the hoop stress (S_{11}) and the through-thickness shear stress (S_{13}). Figure 11 shows the distributions of the hoop stress for the maximum pressure of 459.1 psi. The hoop stresses, which are reacted mainly to the flexural behavior of shell, are high at the sections along the major and minor axes of the elliptical shell where high bending moments created by the external pressure are experienced. The maximum hoop stress is 87,703 psi in compression for the inner fibers at the major axis section and 62,800 psi in tension for the outer fibers. The through-thickness shear stress distribution is shown in Figure 13. As shown, the maximum shear stress is -6,030 psi, which occurs at the neutral axis locations of the cross sections at the transition area of the shell where D-insert support discontinues.

DISTRIBUTIONS OF STRAIN COMPONENTS

The longitudinal (e_{11}), transverse (e_{22}), normal (e_{33}) and through-thickness shear (e_{13}) strain distributions due to the maximum pressure of 459.1 psi for the upper-bound property model are dispatched in Figures 14 to 17 respectively. These strain distributions correspond to the stress contour plots dispatched in Figures 11, 12, 10, and 13 respectively.

The longitudinal strain (e_{11}) distribution at a cross section of the shell is essentially resulting from the combined effects of the flexural deformation caused by the pressure loading and the stretching created by the stack load. As shown in Figure 14, the e_{11} at the upper fibers of the cross section at the flat are in the state of high compression and lower fibers in high tension due to the maximum bending moment acting on the section, while the middle-surface fibers, not affected by bending, are in low tension caused by the stack load. This trend continues with decreasing flexural effect, as the bending moment decreases toward the transition point of the shell. It reaches a section in the midtransition zone where the bending moment becomes zero and only a small tensile strain caused by the stack load remains. Beyond this point, however, the trend picks up again, but with reverse effect. Obviously, the bending moment has changed its sign at this juncture. The reverse bending moment reaches its maximum effect at the end curve of the

shell where the upper fibers of the cross sections are in high tension and inner fibers in high compression. The effect of bending moment reversal can also be observed by reviewing the deformed shape of the shell (Figure 8)--the flat of the shell bends downward while the curve bends outward.

Since there is no direct loading effect in the axial direction of the shell, the transverse strain (e_{22}) distribution shown in Figure 15 is mainly determined by the Poisson's effect of the longitudinal strains (e_{11}). Thus, the e_{22} distribution is similar in trend, but lesser in magnitude and opposite in direction to that of e_{11} (Figure 14). Note that a Poisson's ratio of 0.3 was used for all three material directions in the analysis.

The normal strain (e_{33}) distribution is mainly determined by the direct compression effect caused by the pressure loading, in combination with the Poisson's effect of the longitudinal strains. As shown in Figure 16, this results in a normal strain distribution that is predominantly compressive but retains some small tensile regions at the upper fibers of the flat and the inner fibers of the curve where high compressive, longitudinal strains caused by bending effects are at their maxima. However, the normal strain distribution at the inner surface region of the curve is greatly affected by the gapping created at the shell and D-insert interface by the high pressure. The gradient of the strain distribution at this area is quite high, especially at the area just beyond the remaining D-insert contact where the maximum tensile strain occurs, as shown in Figure 16.

Consistent with the shear stress (S_{13}) distribution shown in Figure 13, the through-thickness shear strain distribution (e_{13}) shown in Figure 17 indicates that the maximum shear strain occurs at the neutral axis locations of the cross sections in the transition area of the shell.

COMPARISON OF STRAIN DATA

Figure 1 shows the locations and orientations of the two types of strain gages that were placed on the Shell 010 for strain measurements in the pressure-plus-stack load test. Gages of type CEA-06-062UR-350 are small 45° rectangular single-plane rosettes aligned with the circumferential and radial directions on the cross sectional end of the shell for longitudinal (e_{11}), normal (e_{33}) and through-thickness shear (e_{13}) strain measurements. Gages of type CEA-13-125WT-350 are two-element 90° "tee" stacked rosettes aligned with circumferential and axial directions on the inside surface of the shell for longitudinal (e_{11}) and transverse (e_{22}) strain measurements. Eighteen strain gages are instrumented at the critical locations of the shell that includes the flat, the midtransition and the transition areas, as shown in Figure 1. The calculated strain values at the corresponding nodes of the upper- and lower-bound property FEMs are compared with the test data reported by Maltby (1991). As shown in Figures 18 to 35, the calculated strains for the simulated pressure load increments in load step 2 are plotted against the recorded strain versus stack stress curves for several cycles of stack and pressure loadings. Noted that the calculated strain values for stack preloading (load step 1) are omitted from the plots for clarity.

These figures show the predicted strain values for the upper-bound property model correlated better with the test data than the lower-bound ones. Table 3 summarizes the quality of strain data correlations between the predicted values for the upper-bound property model and the test results.

In general, the predicted values of strain components for the upper-bound property model correlated very well with the test data at all the locations considered. Figures 18 to 35 show the strain components calculated by FEMs not only have the same signs as the test data, but also show the similar trends with respect to the increasing pressure. However, the correlation for the magnitudes of the interlaminar shear strains (e_{13}) at areas surrounding the shell and D-insert contact are mostly fair only. This discrepancy may be attributed to several reasons as follows:

1. Uniform shear modulus (G_{13}) was assumed throughout the entire thickness of the current shell model. This estimated property may be low for the inner surface of the composite shell whose material properties may vary through the thickness.

2. Figure 17 shows the strain gradient at the inner shell surface area surrounding the D-insert contact are steep due to the strss concentration effect. The rather coarse and uniform mesh of the current FEM may not provide ABAQUS with an adequate resolution to accurately calculate a nodal strain value, which is averaged over the elements connected to the node in ABAQUS analysis.

3. Strains are calculated at a point in the FEA, but they are measured over a finite length (0.062 inch for the rectangular type gages) in the test. An inherent error between the two exists.

Table 3. Quality of Strain Data Correlations For Upper-Bound Property Model

Zone	Strain Gage	Node No.	Fig. No.	e_{11} (LONG.)	e_{33} (NORM.)	e_{13} (SHEAR)	e_{22} (TRANS.)	Remarks
F								
L	M1IM/M2IM	1	18/19	Fair/Good	NA	NA	Good	Biaxial Gages
A	MXAI	7	20	Good	Very Good	Good		No shear strain
T	MXAM	126	21	Good	Good	Good		No shear strain & others are small
	MTXAI	521	22	Good	Good	Poor		
	MTXAM	604	23	Good	Very Good	Good		
T	T2XAI/T2XBI	958	24/25	Very Good	Very good	Good		
R	T2XAM	1022	32	Good	Fair	Fair		
A							Very	
N	TD1IM/TD2IM	963	26/27	Very Good	NA	NA	Good	Biaxial Gages
S	TDXAI/TDXBI	969	28/29	NA/Good	Very Good	NA/Fair		
I	TDXAM/TDXBM	1026	30/31	Very Good	Very Good	Good/Fair		
T	TDXAO	1104	33	Fair	Good	Good		
I								
O	T1XAI	1115	35	Good	Good	Fair		
N	T1XAM	1134	34	Very Good	Good	Fair		

Ranking: Very Good--Predicted values within 5% of Test Data
Good--Predicted values within 10% of Test Data
Fair--Predicted values within 25% of Test Data
Poor--Predicted values greater than 50% of Test Data
NA--Test Data not available

Comments: (1) Good to very good correlations for longitudinal strains (e_{11}) at all locations, except node 1104 where the correlation was only fair.

(2) Good to very good correlations for normal strains (e_{33}) at all locations, except node 1022 where the correlation was only fair.

(3) Good to fairly good correlations for shear strains (e_{13}) at all locations, except node 521 where the correlation was poor.

CONCLUSIONS AND RECOMMENDATIONS

The transducer shell FEM constructed with ABAQUS' 20-node solid elements using linear, homogeneous, and orthotropic "smeared" material properties has predicted the global response and strain distribution of the loaded shell that correlate well with the test data obtained from the stack load and hydrostatic pressure tests. The model should provide a good base model for the sensitivity study of the shell's structural performance to thickness variation and to nonuniform material property distribution in the shell resulting from the variation in parameters, such as moduli of the constituents, fiber volume fraction and ply arrangement of the laminate. However, the model needs to be refined at areas in contact with the D-insert, as well as to simulate nonlinear material behaviors that were observed in the pressure tests. The effects of variations in longitudinal and through-thickness properties (E_{11} and G_{13}) on the flexural behavior of the shell, which is vital to the acoustic performance of the flextensional transducer, must be investigated further.

As predicted by the FEMs, a gap formed at the shell and D-insert interface when the shell was pressurized beyond 400 psi in the tests. Gapping has an adverse effect on the acoustic performance of the transducer shell and can reduce the fatique life of the shell. It must be prevented.

Finally, a stress analysis cannot be concluded without mentioning the issue of failure. Failure criteria are more complex in composites, which can delaminate or have either fiber or matrix failure. The problems in defining failure modes for the composite shell and the issue of what constitutes a proper failure criterion in predicting reasonable fatigue life for the transducer shell must be addressed in future work.

REFERENCES

Halpin, J. C., 1984. "Primer On Composite Materials: Analysis," Technomic Publishing Company, Inc.

MacNeal-Schwendler Corporation, January 1989. "MSC/NASTRAN Application Manual," Vol.1, Sec.2.12.

Maltby, J. D., 2 June 1988. "Composite Transducer; Material Properties Prediction," NRaD Memorandum Ser 932/88-88.

Maltby, J. D., 3 Sept 1991. "Natural Frequency Data of Composite Flextensional Shells," NRaD Memorandum Ser 932/39-91.

Maltby, J. D., October 1991. "Static Structural Test On Composite Flextensional Transducer Shells," NRaD Technical Report 1447.

Rouse, N. E., 25 February 1988. "Optimizing Composite Design," Machine Design, pp. 62-66.

Shaw, R. C., 16 May 1989. "Review of MSC/NASTRAN Analysis Capability For Laminated Composite Materials," NRaD Memorandum Ser 931/41-89.

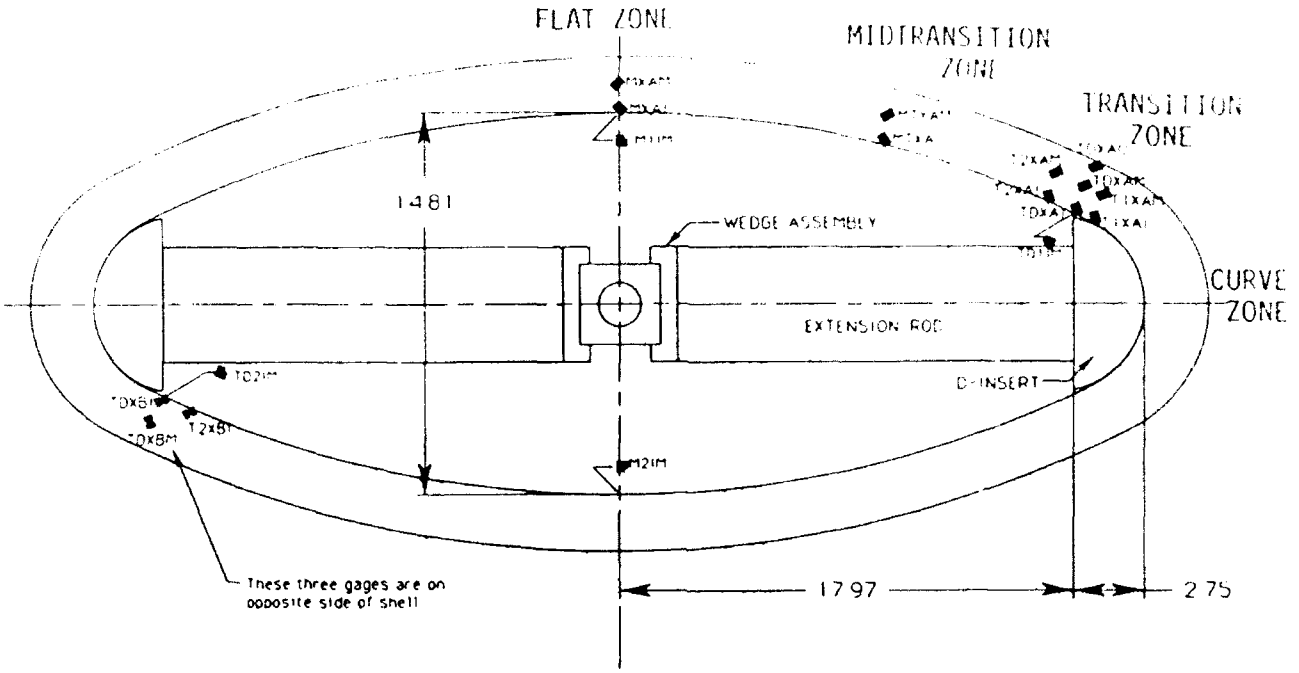

Figure 1. Test configuration of Shell 010 showing strain gage locations.

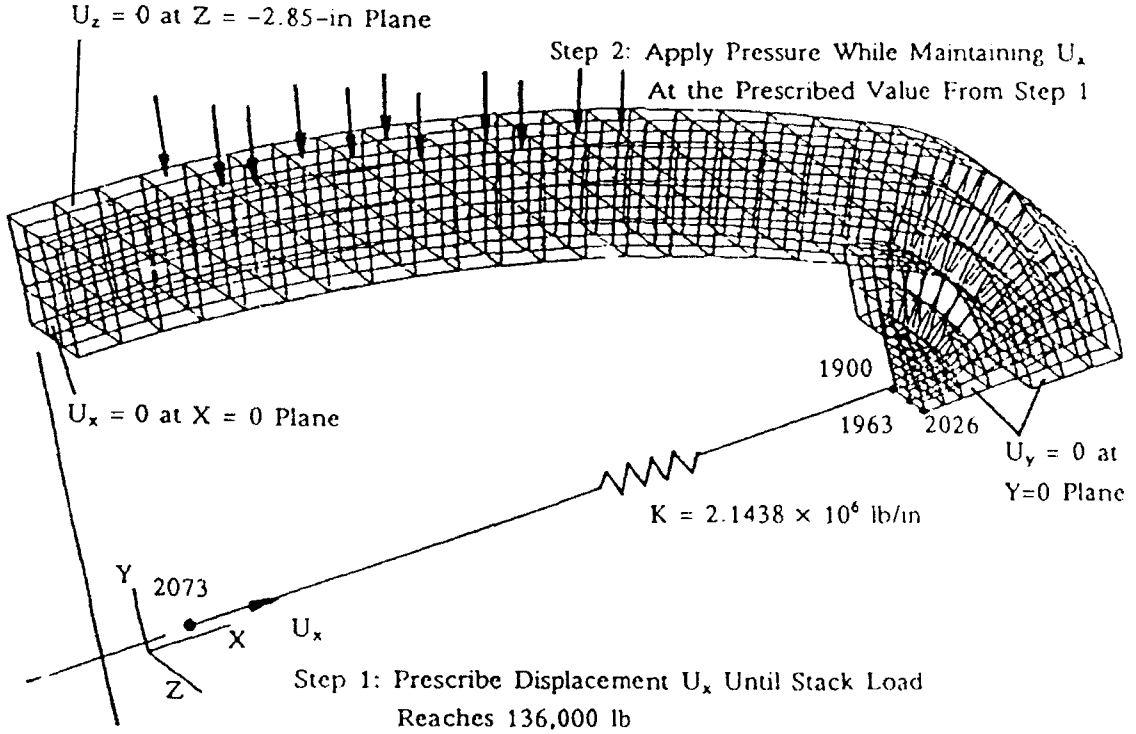

Figure 2. Transducer FEM with boundary and two-step loading conditions simulating stack load and hydrostatic pressure tests.

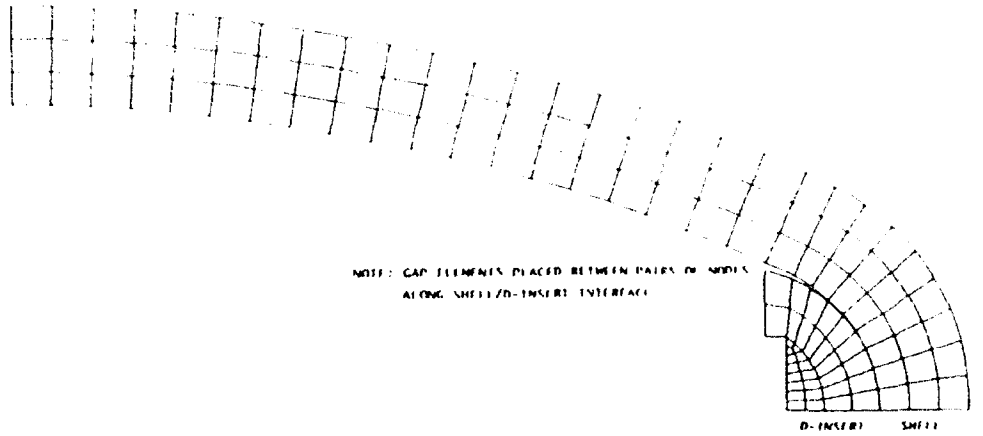

Figure 3. Section view of transducer FEM showing shell and D-insert interface.

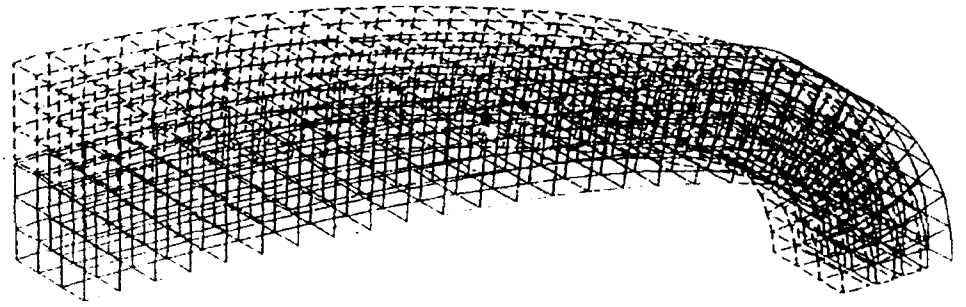

Figure 4a. First flexural mode of shell.

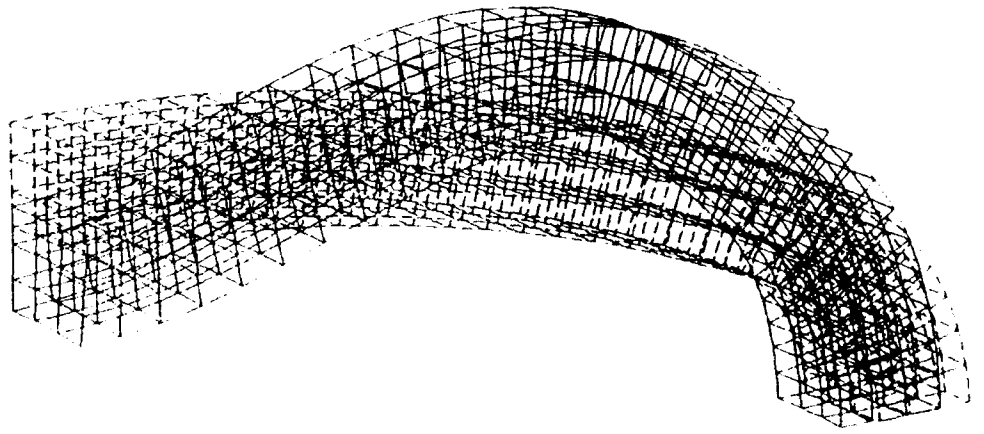

Figure 4b. Second flexural mode of shell.

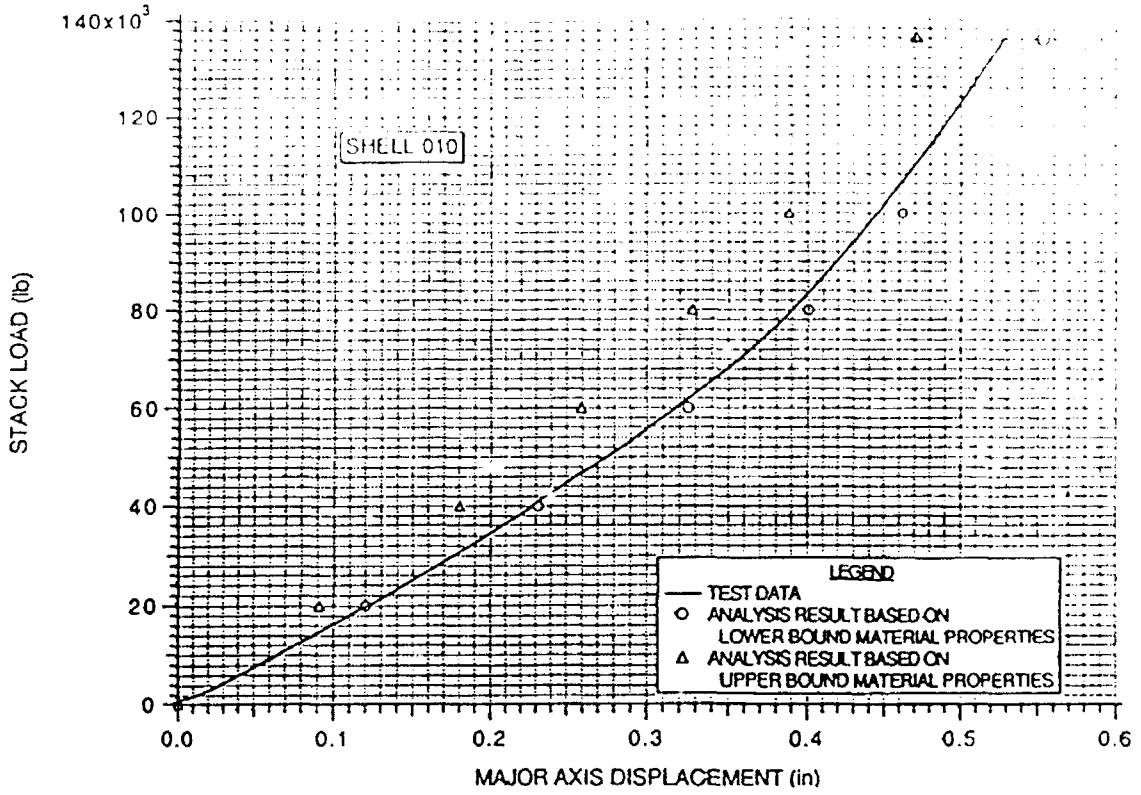

Figure 5a. Stack preload versus major axis displacement.

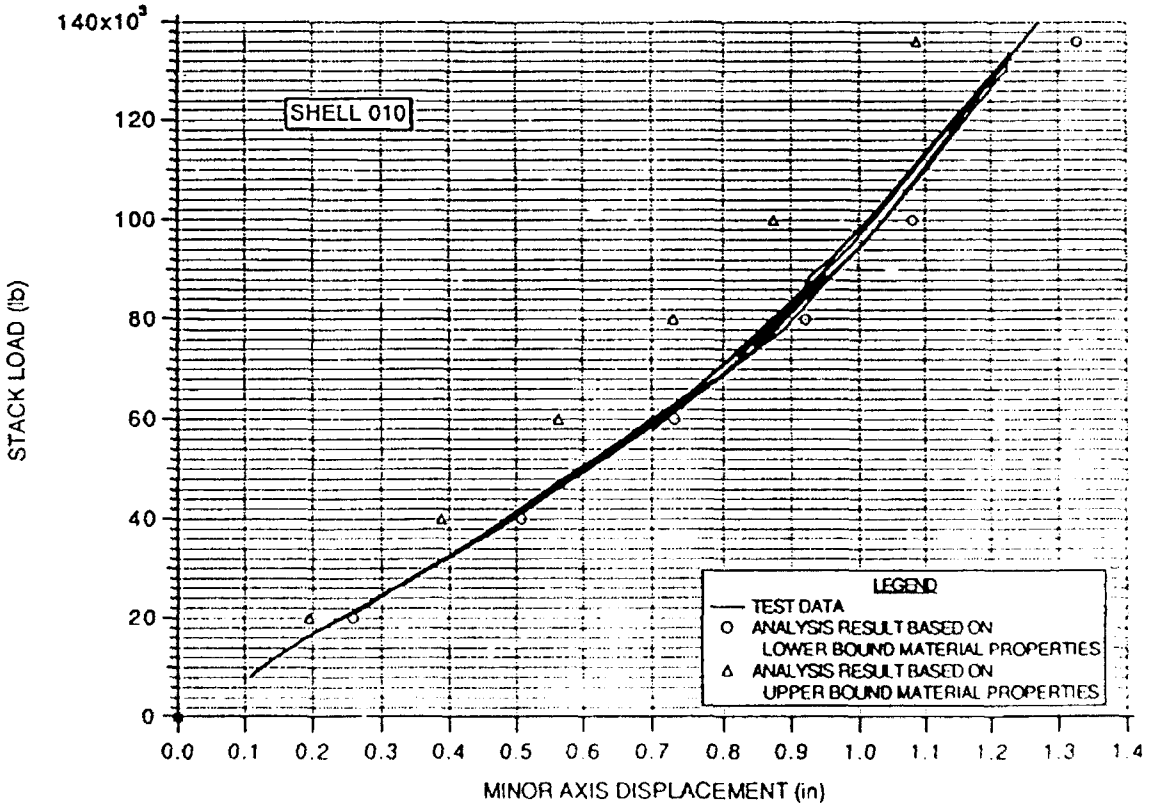

Figure 5b. Stack preload versus minor axis displacement.

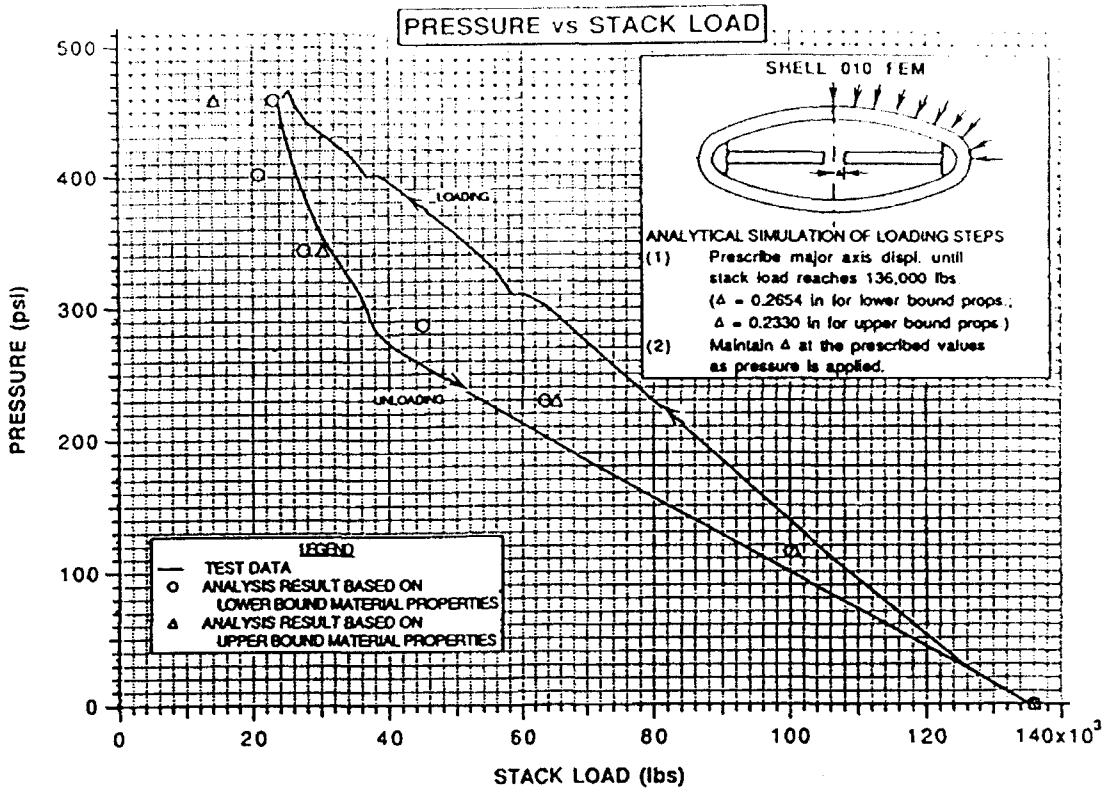

Figure 6. Stack load versus hydrostatic pressure.

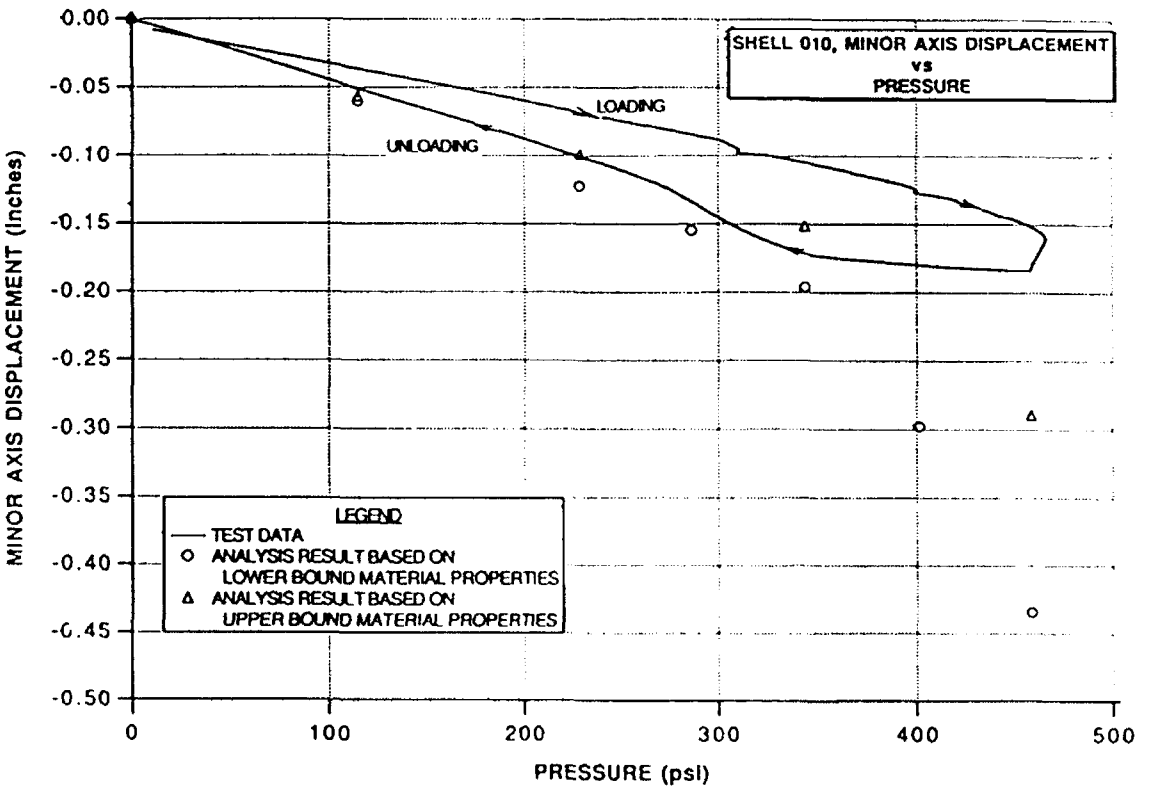

Figure 7. Pressure load versus minor axis displacement.

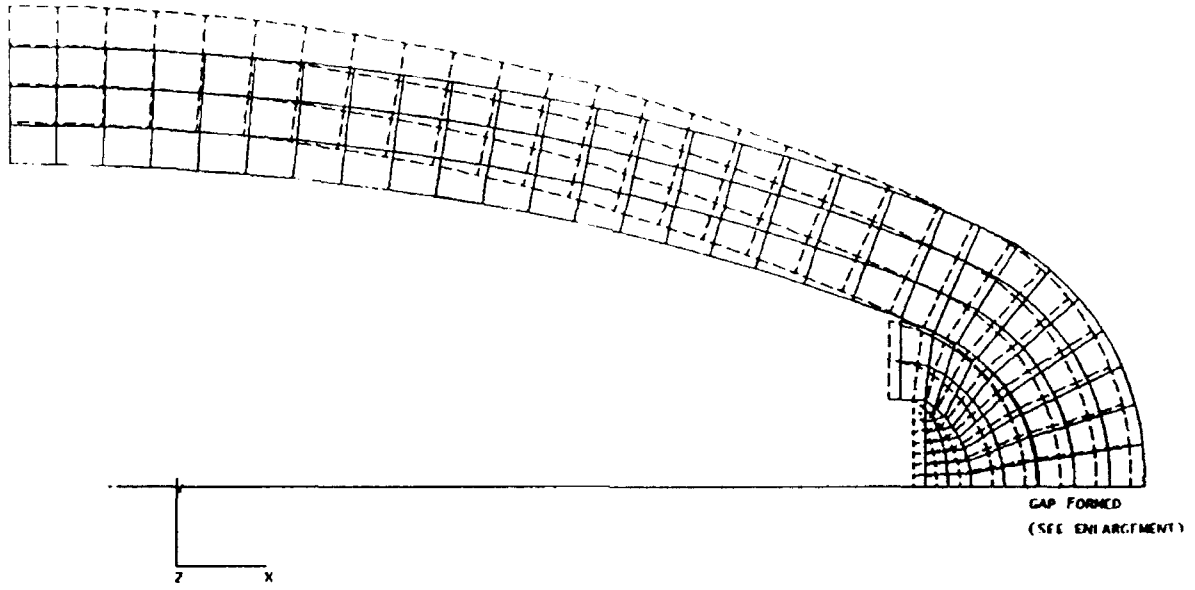

Figure 8. Deformed shape of Shell 010 due to 459-psi pressure.

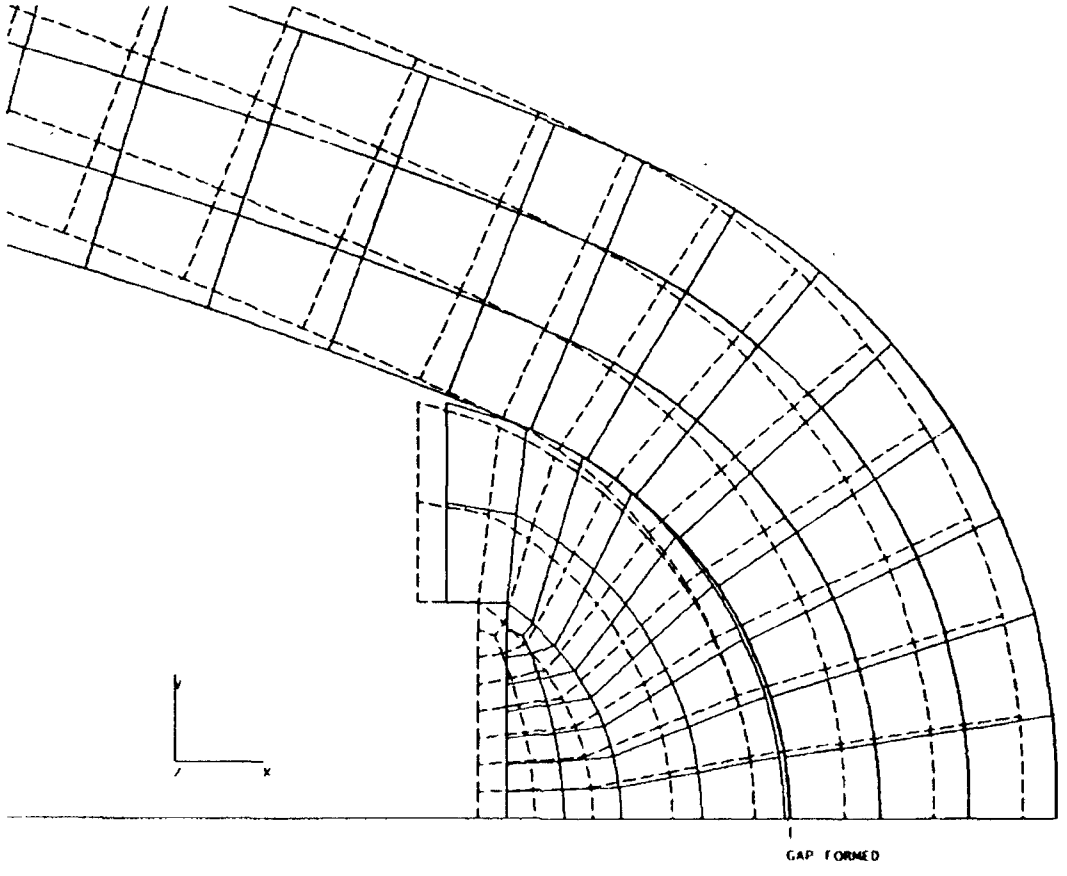

Figure 9. Enlarged view of deformed shell and D-insert interface under 459-psi pressure.

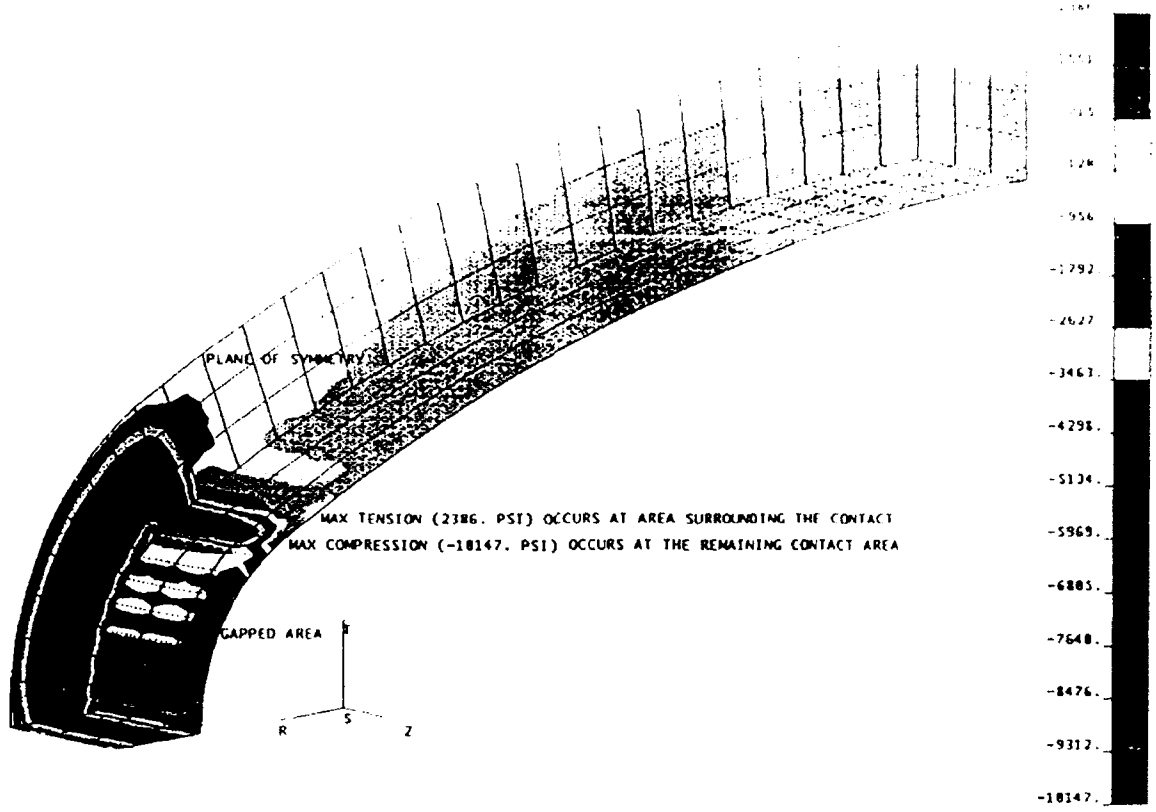

Figure 10. Radial stress (S_{33}) distribution due to 459-psi external pressure.

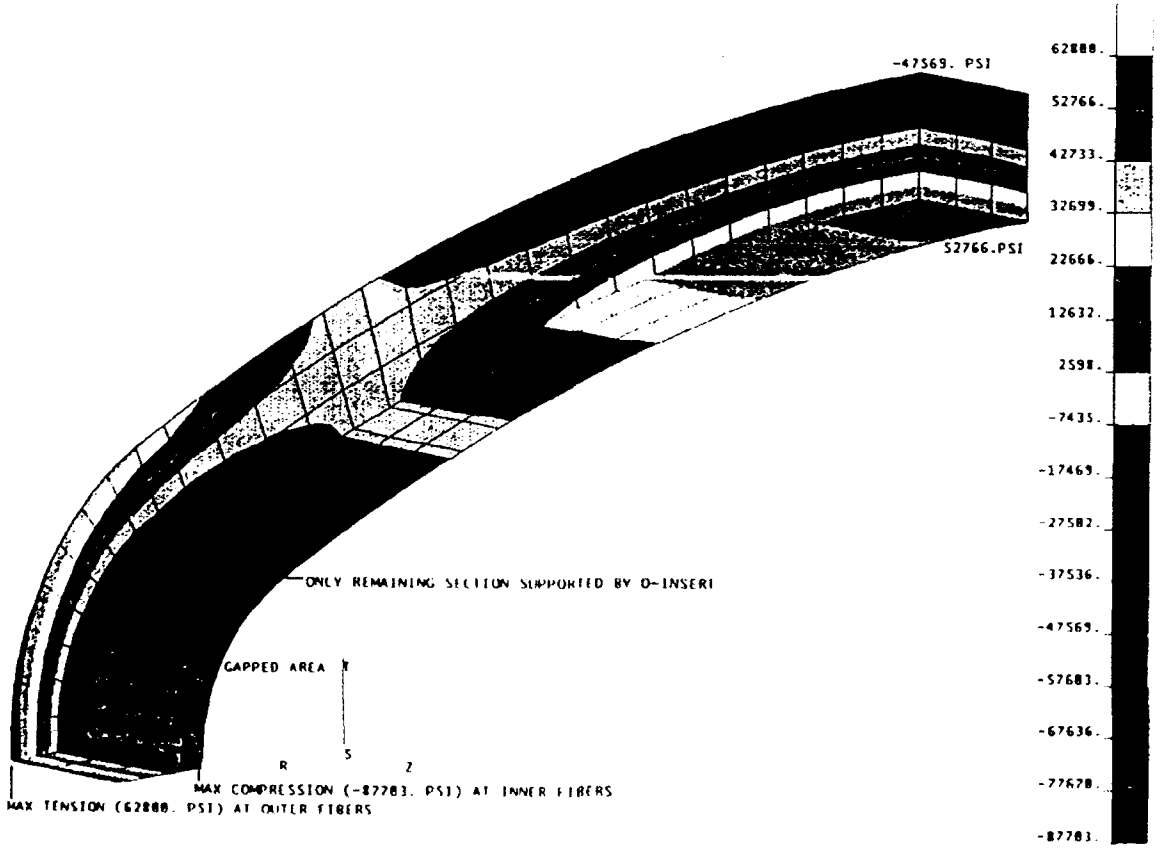

Figure 11. Hoop stress (S_{11}) distribution due to 459-psi external pressure.

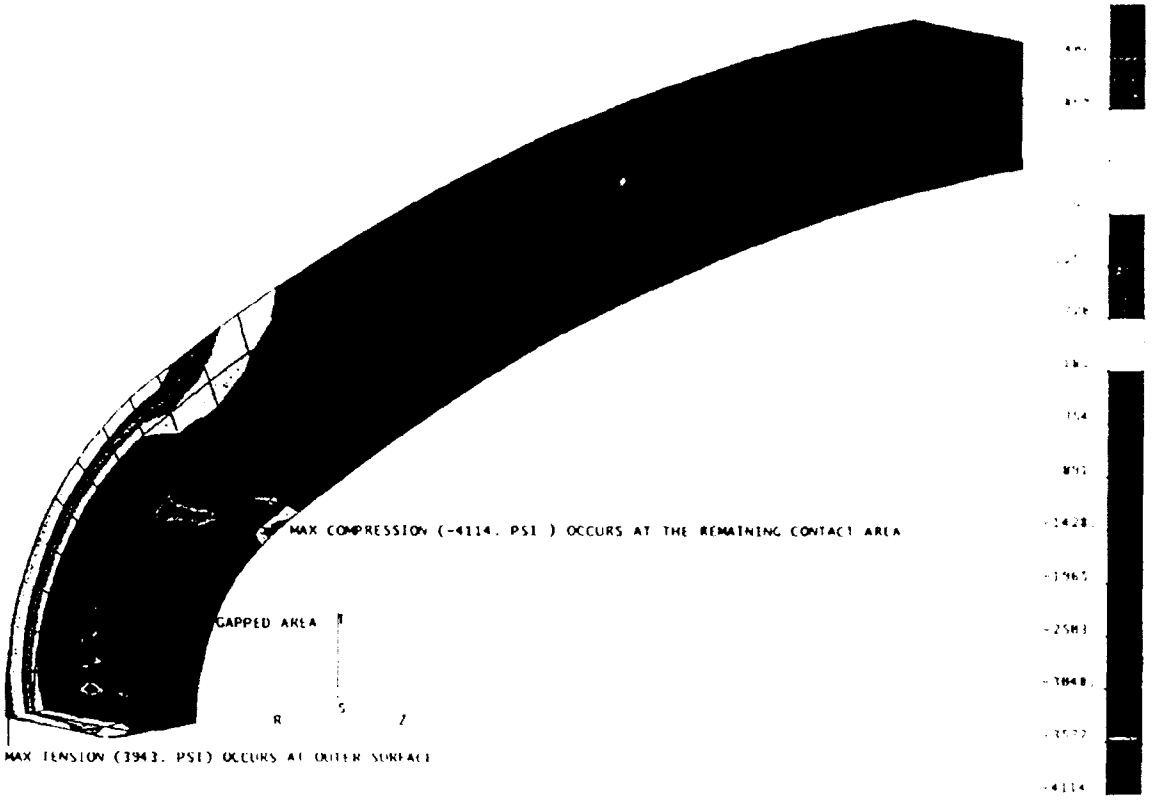

Figure 12. Transverse stress (S_{22}) distribution due to 459-psi external pressure.

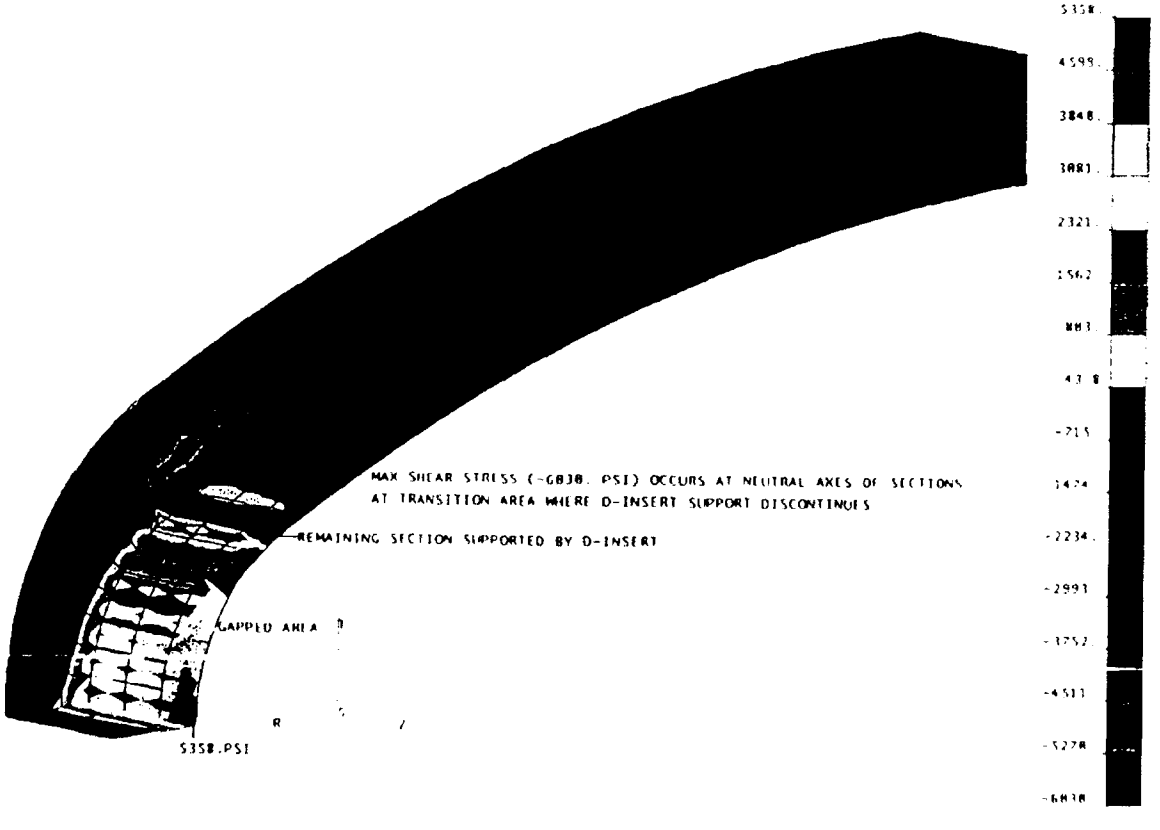

Figure 13. Through-thickness shear stress (S_{13}) distribution due to 459-psi external pressure.

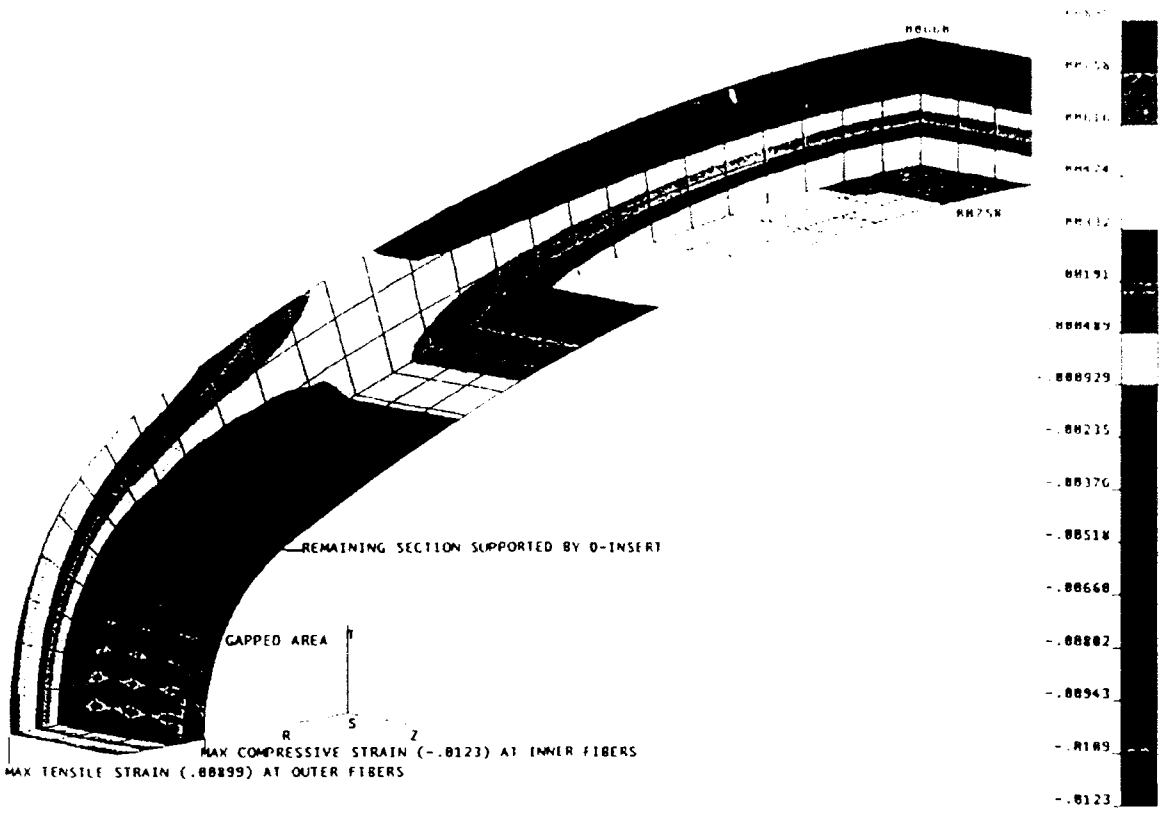

Figure 14. Longitudinal strain (e_{11}) distribution due to 459-psi external pressure.

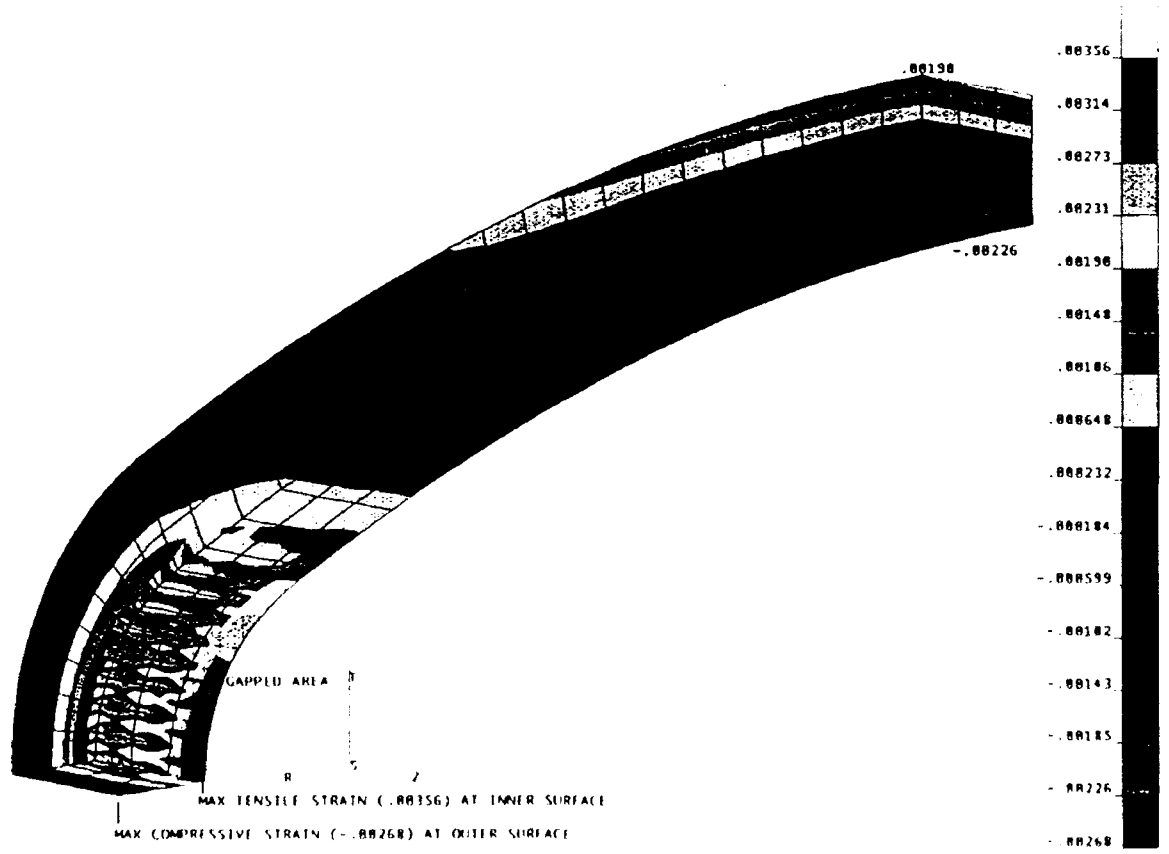

Figure 15. Transverse strain (e_{22}) distribution due to 459-psi external pressure.

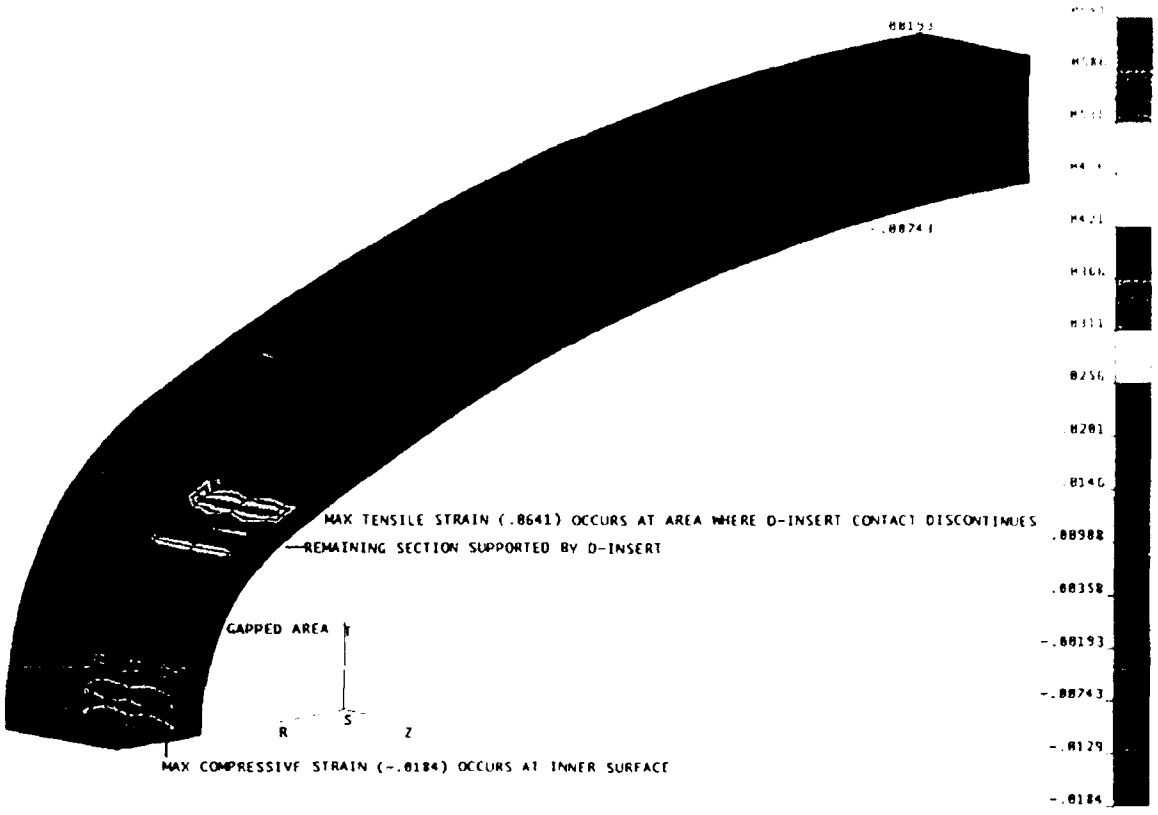

Figure 16. Normal strain (e_{33}) distribution due to 459-psi external pressure.

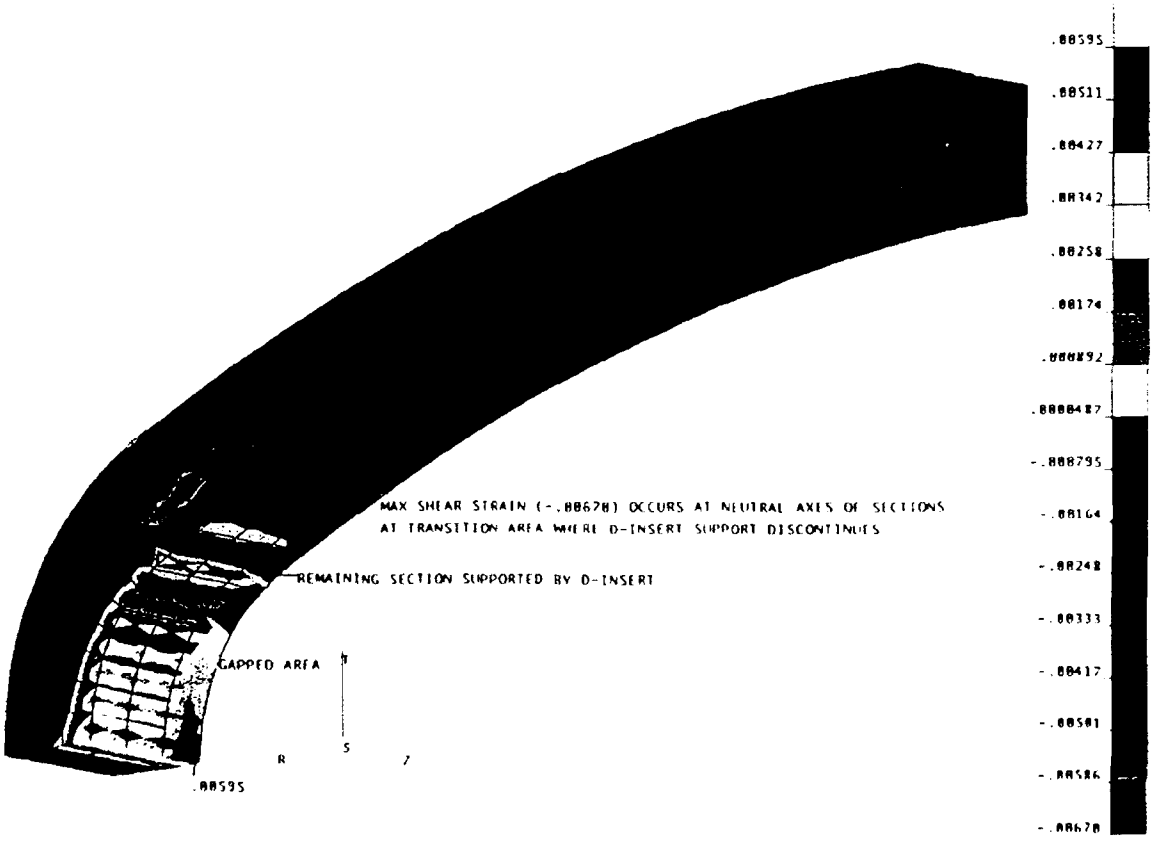

Figure 17. Through-thickness strain (e_{13}) distribution due to 459-psi external pressure.

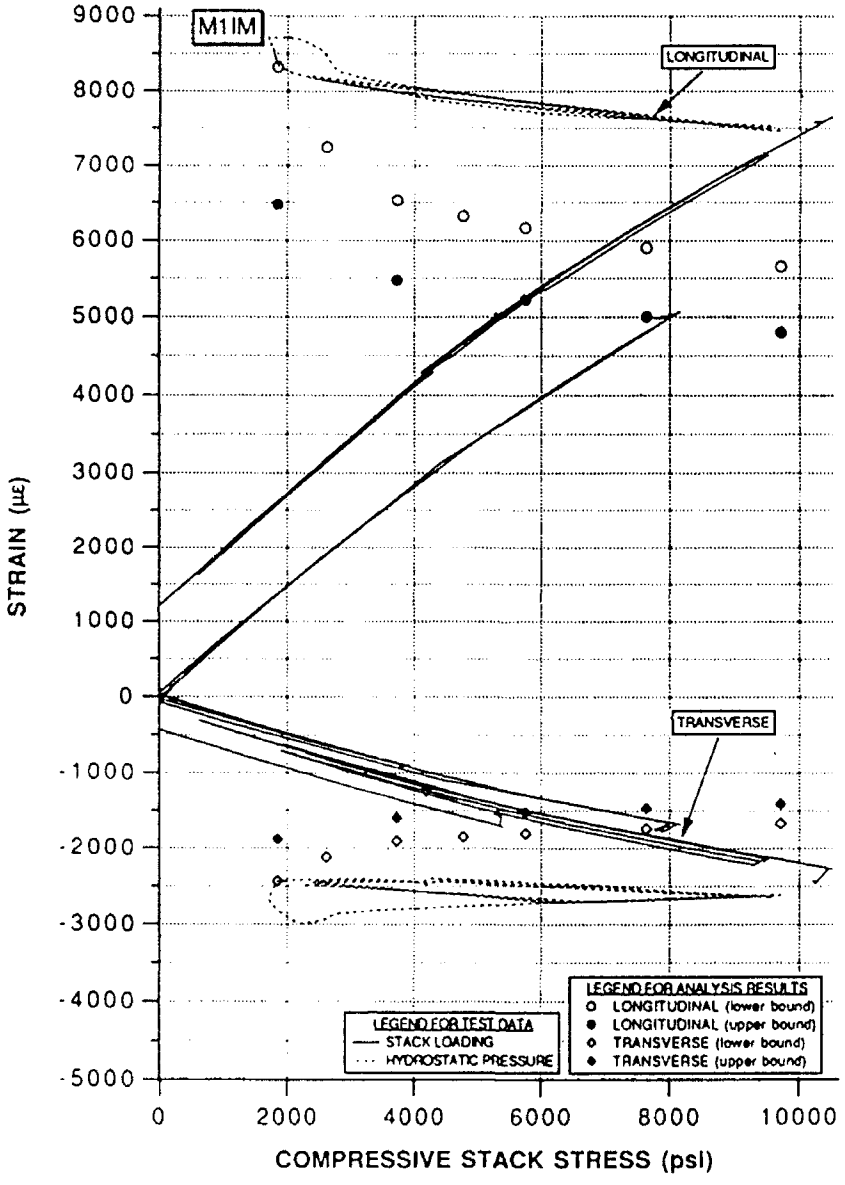

Figure 18. Strain data comparison (Node 1 versus M1IM).

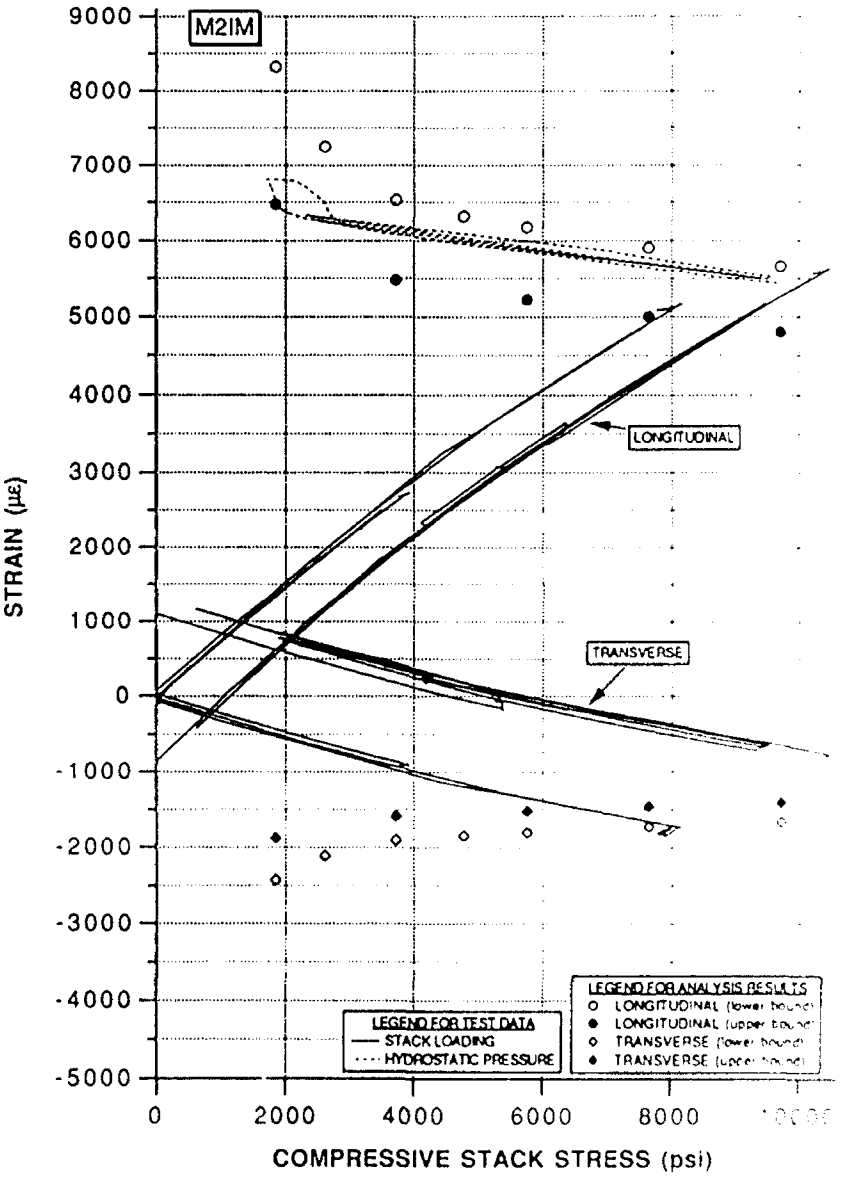

Figure 19. Strain data comparison (Node 1 versus M2IM).

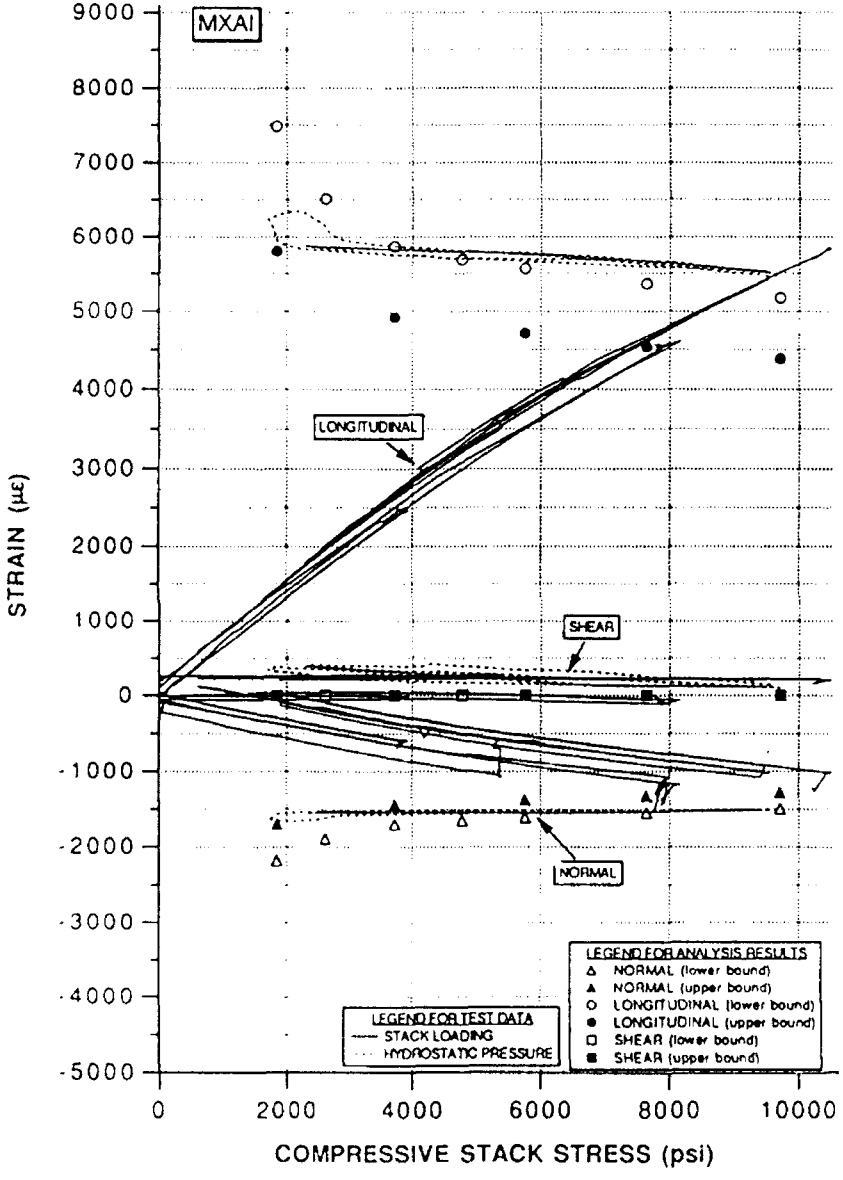

Figure 20. Strain data comparison (Node 7 versus MXAI).

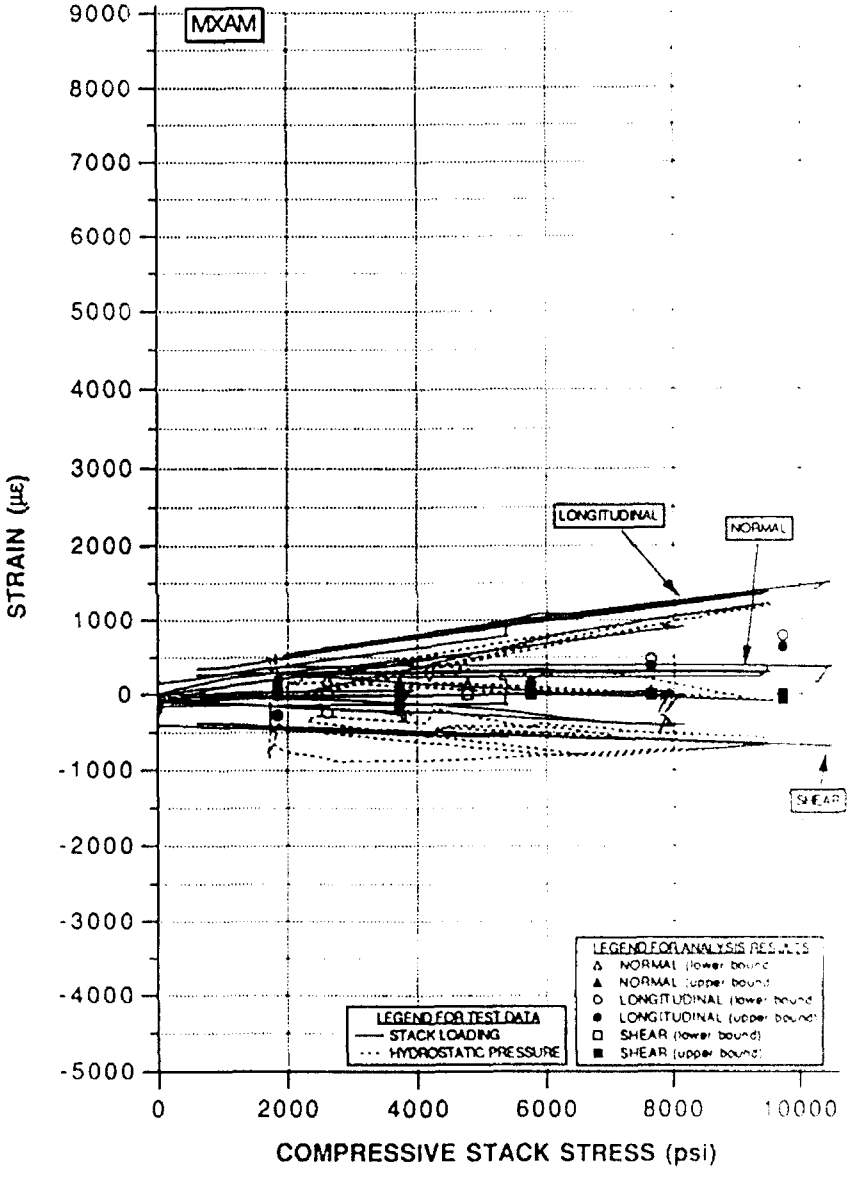

Figure 21. Strain data comparison (Node 126 versus MXAM)

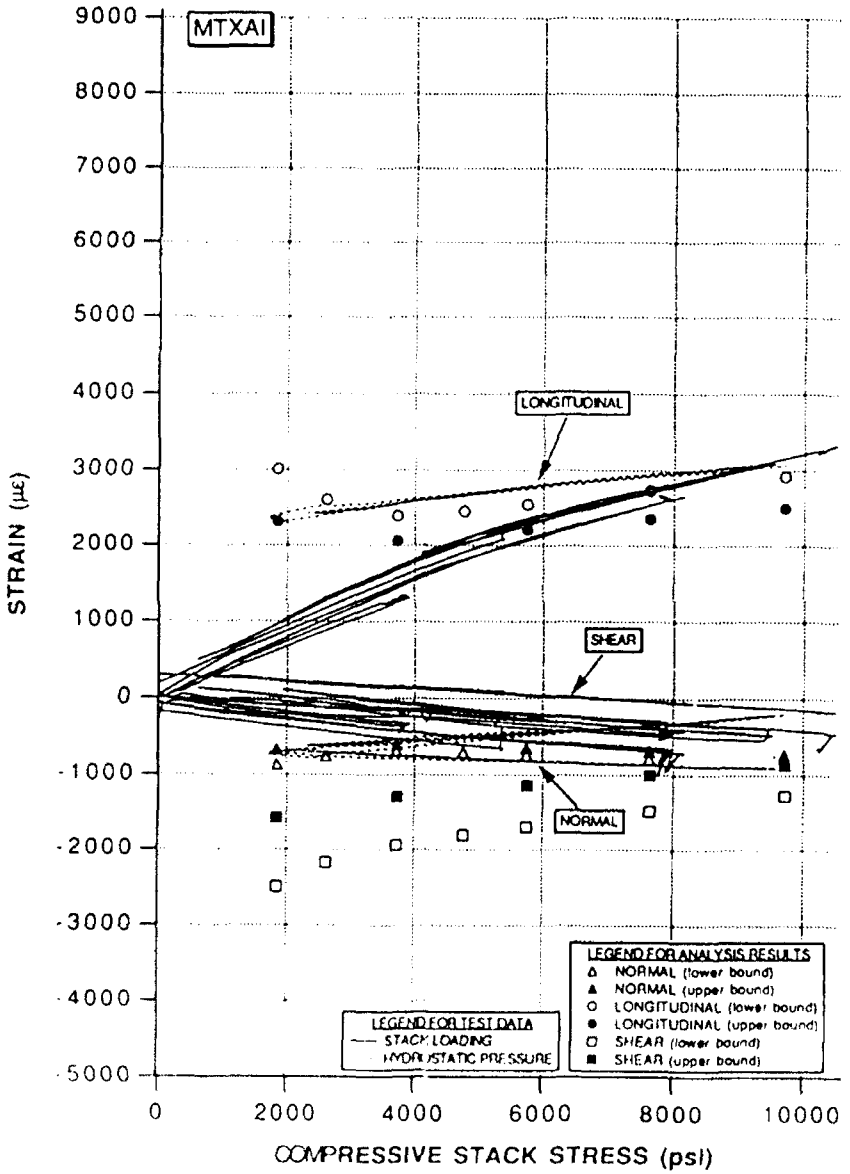

Figure 22. Strain data comparison (Node 521 versus MTXAI).

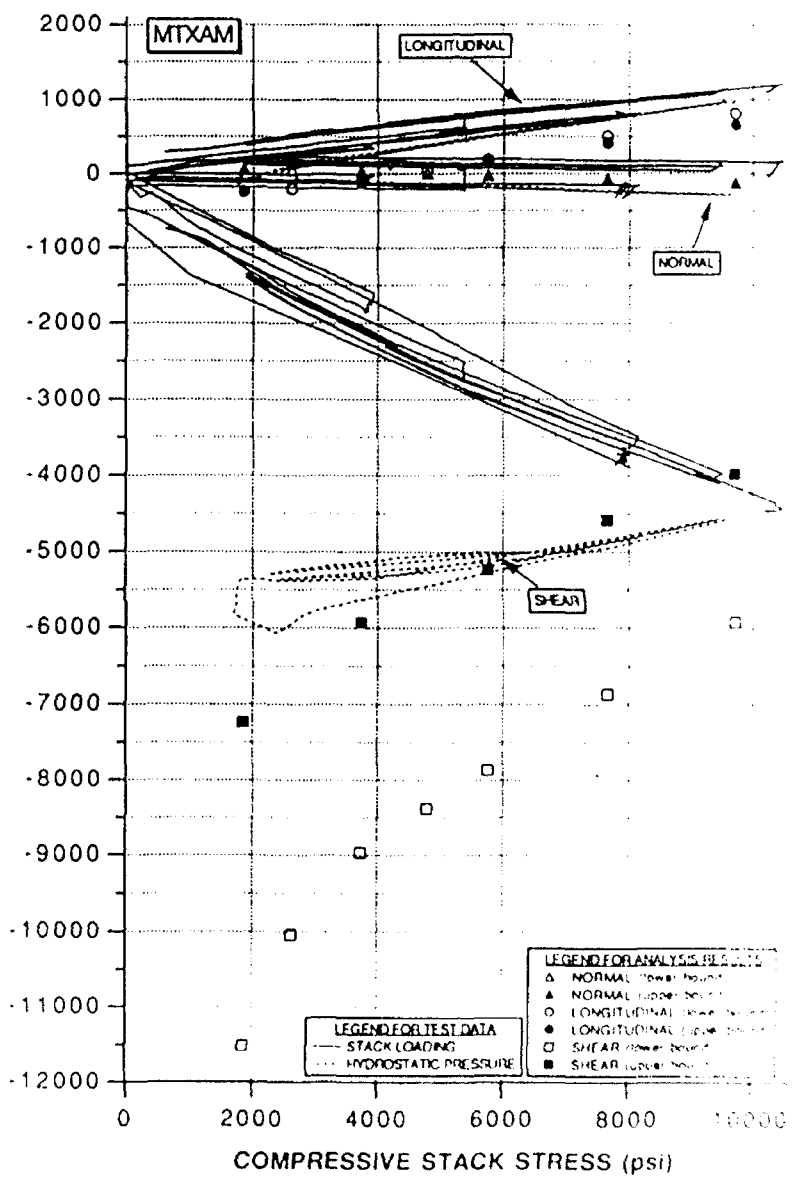

Figure 23. Strain data comparison (Node 604 versus MTXAM).

THIS
PAGE
IS
MISSING
IN
ORIGINAL
DOCUMENT

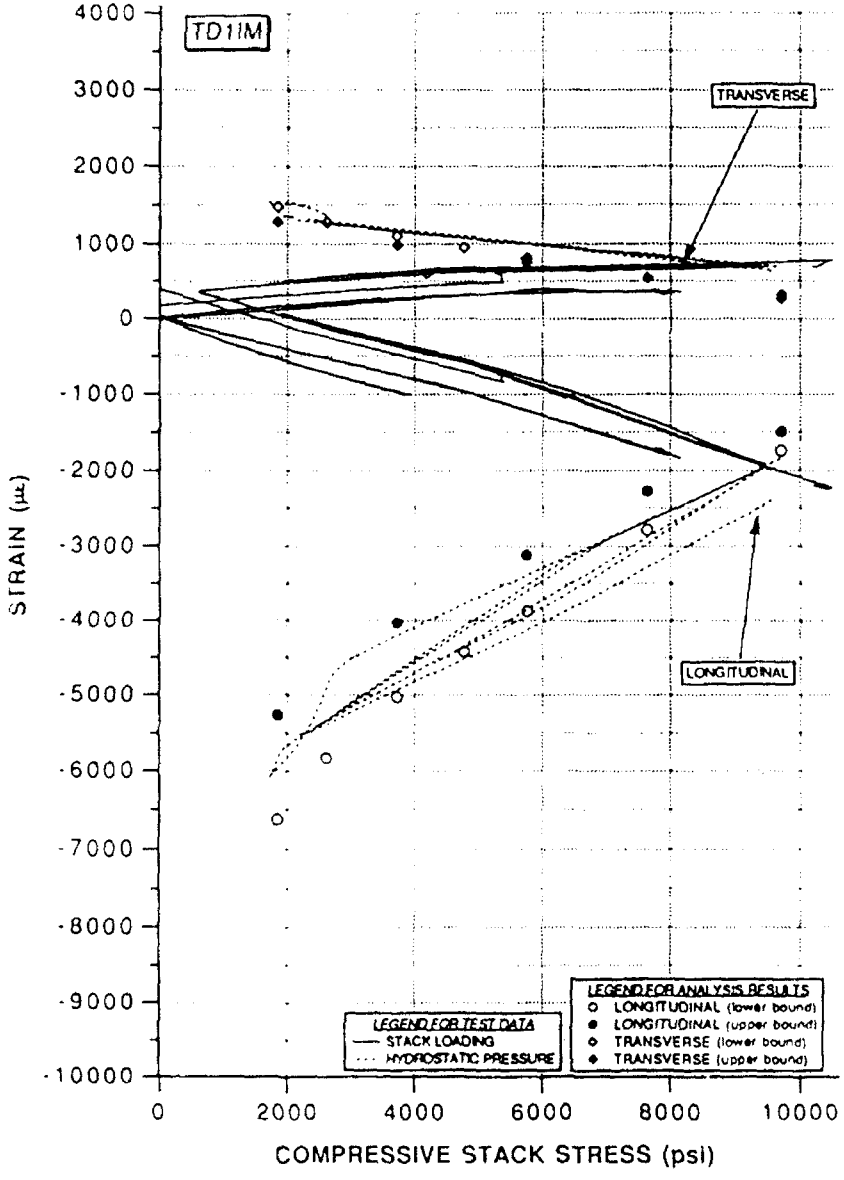

Figure 26. Strain data comparison (Node 963 versus TD1IM).

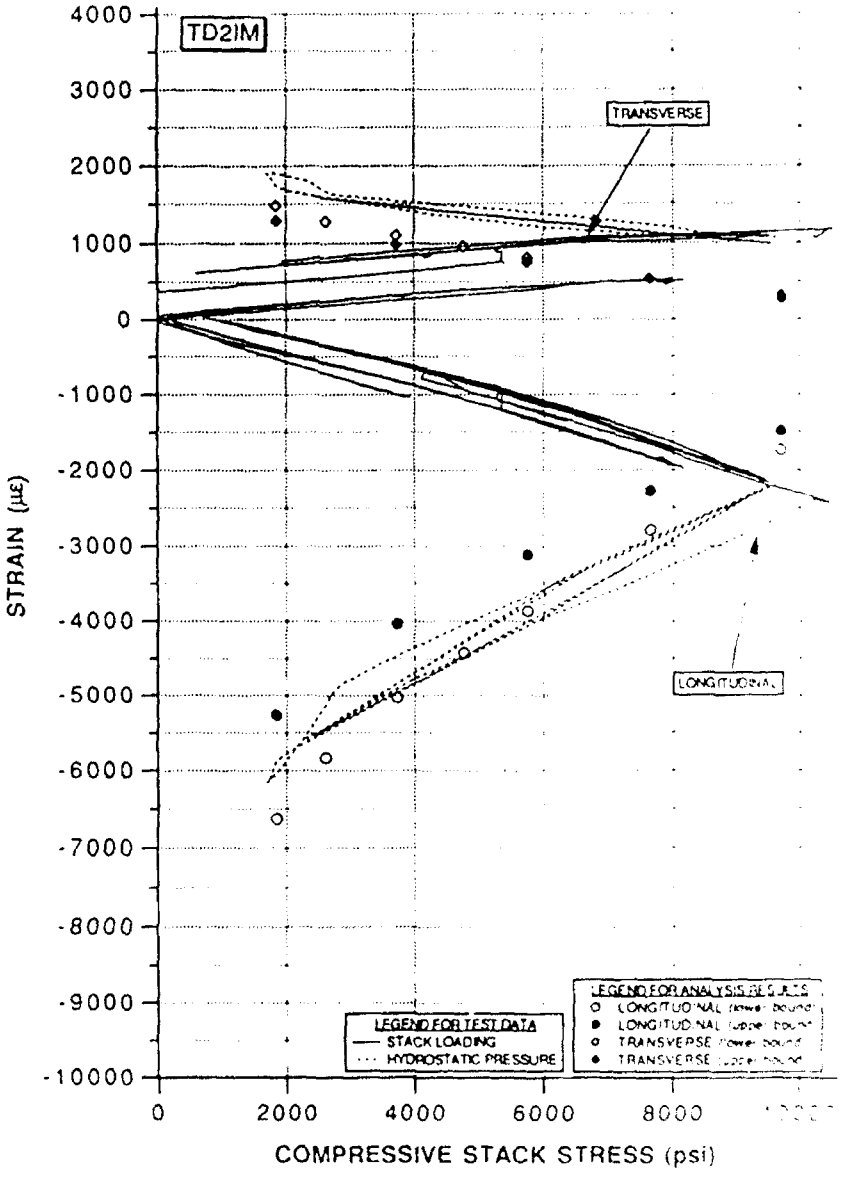

Figure 27. Strain data comparison (Node 963 versus TD2IM).

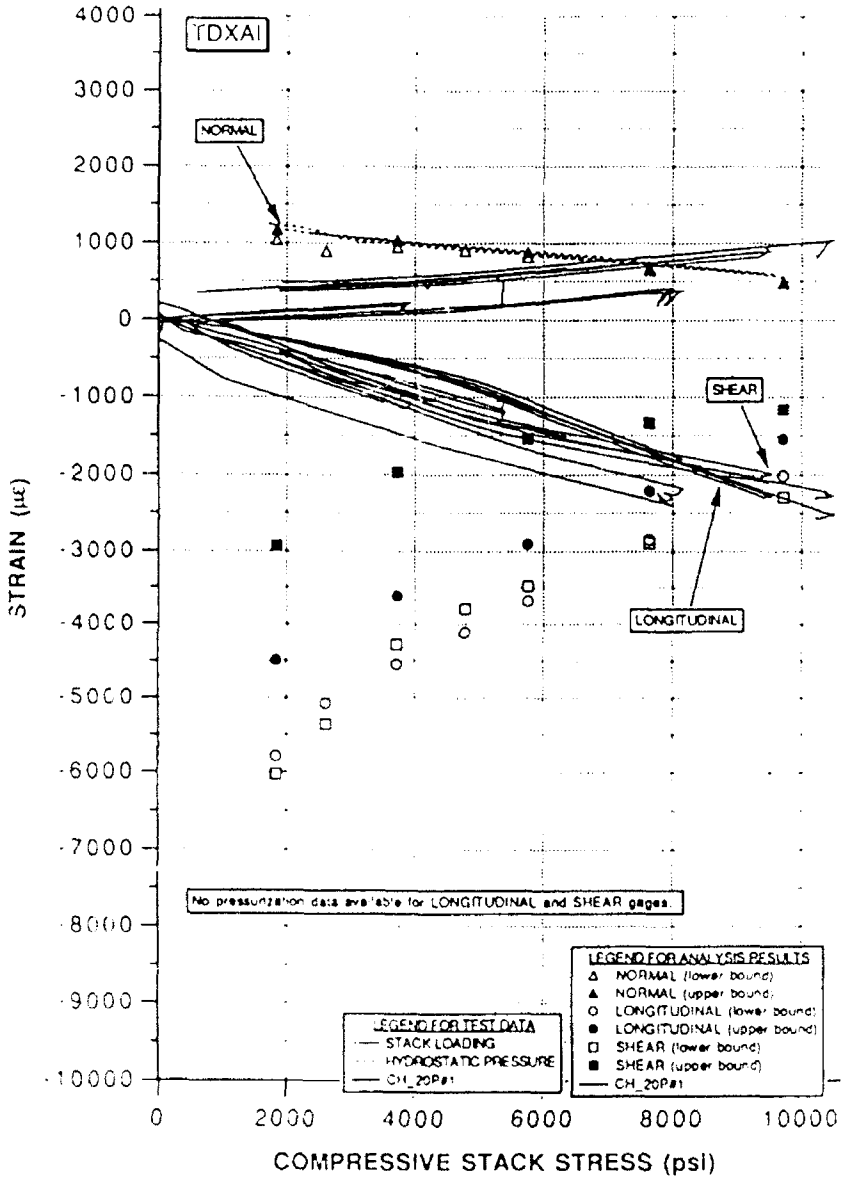

Figure 28 Strain data comparison (Node 969 versus TDXAI).

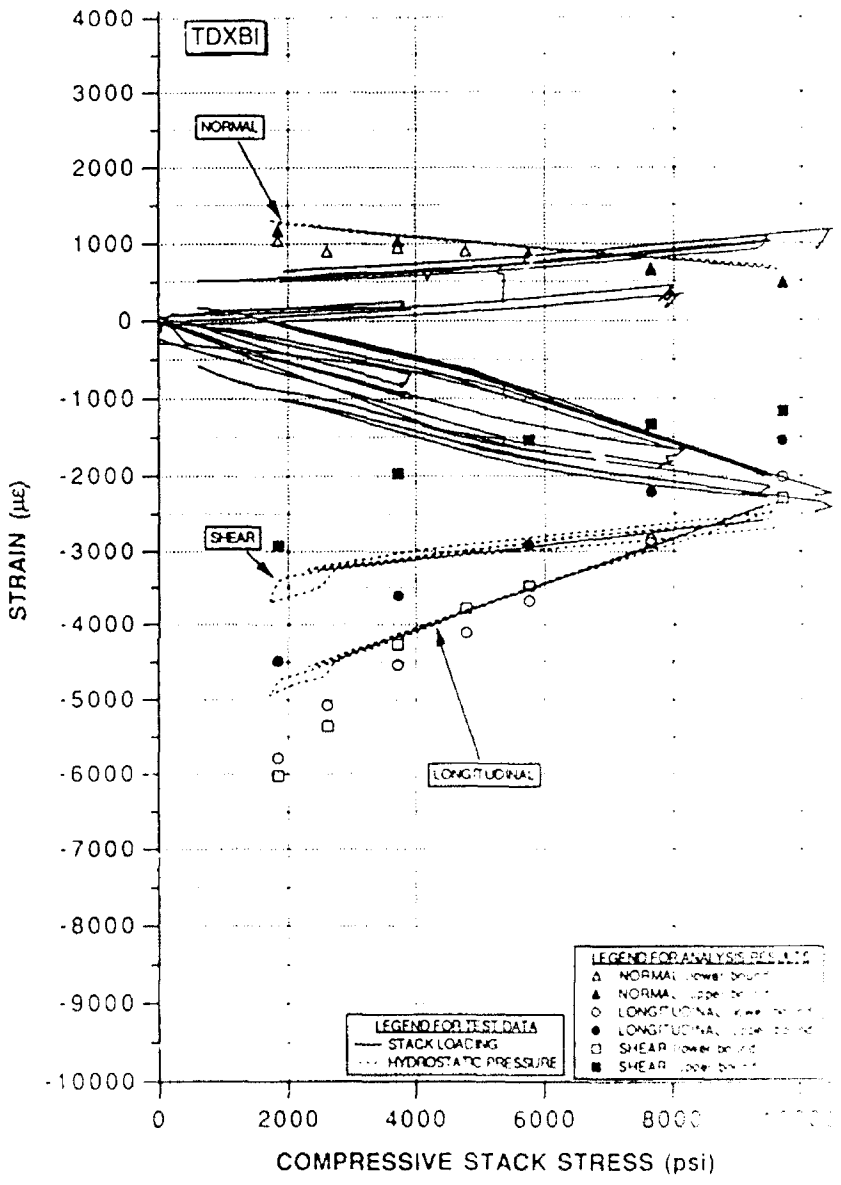

Figure 29 Strain data comparison (Node [illegible] versus TDXBI).

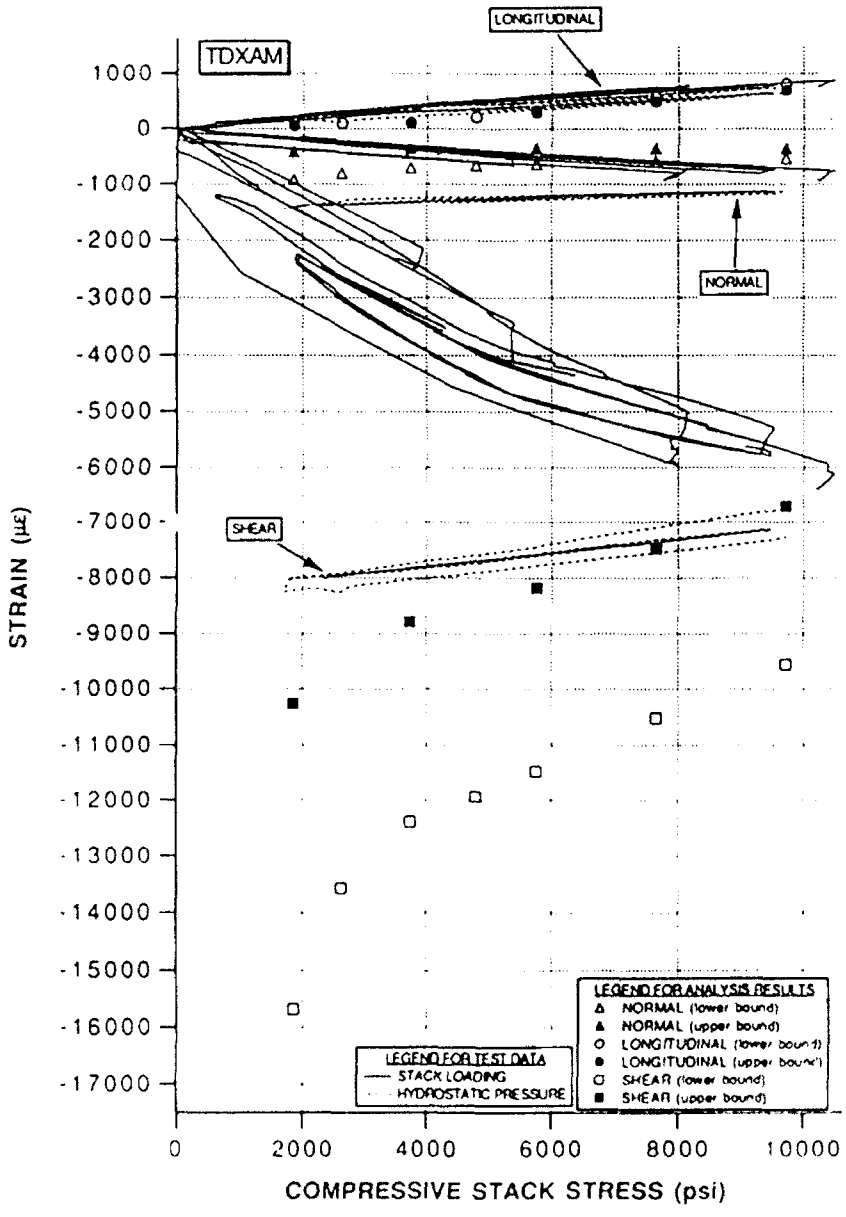

Figure 30 Strain data comparison (Node 1026 versus TDXAM)

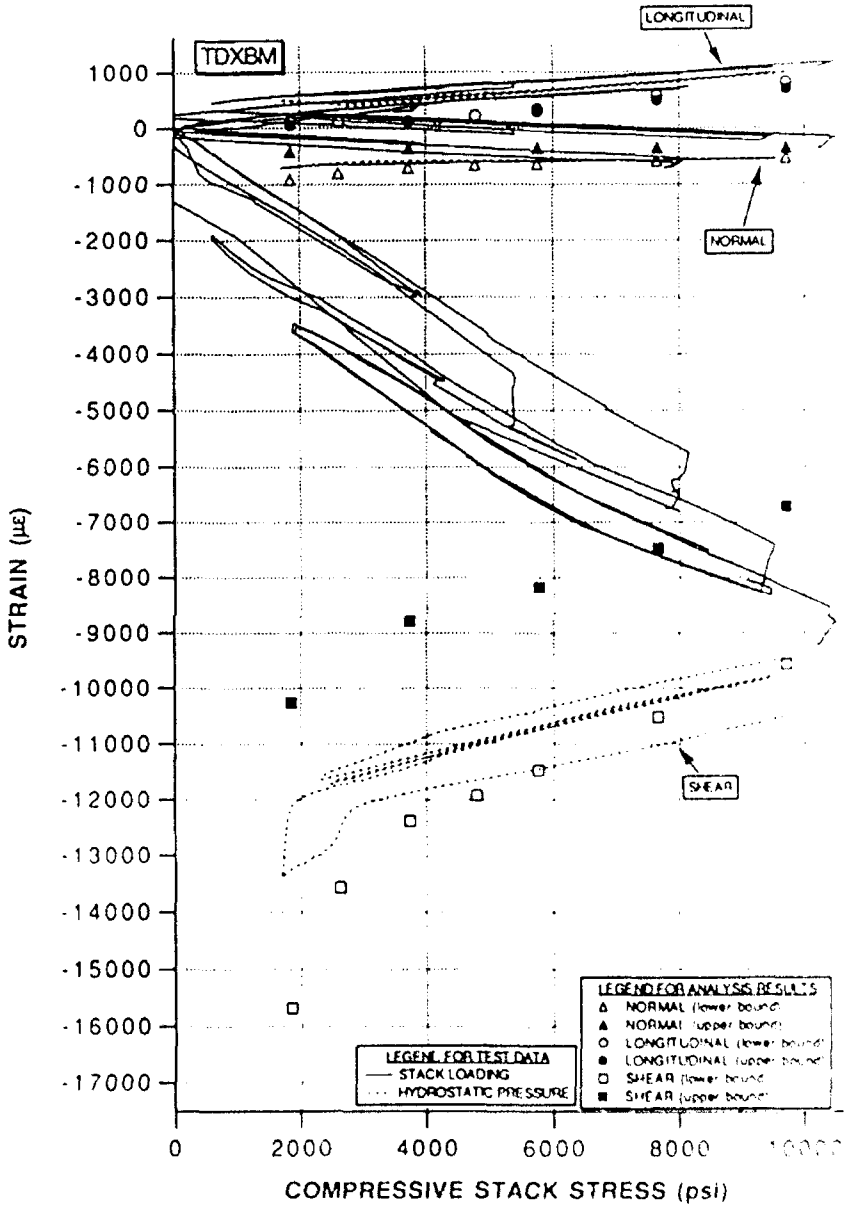

Figure 31. Strain data comparison (Node 1026 versus TDXBM

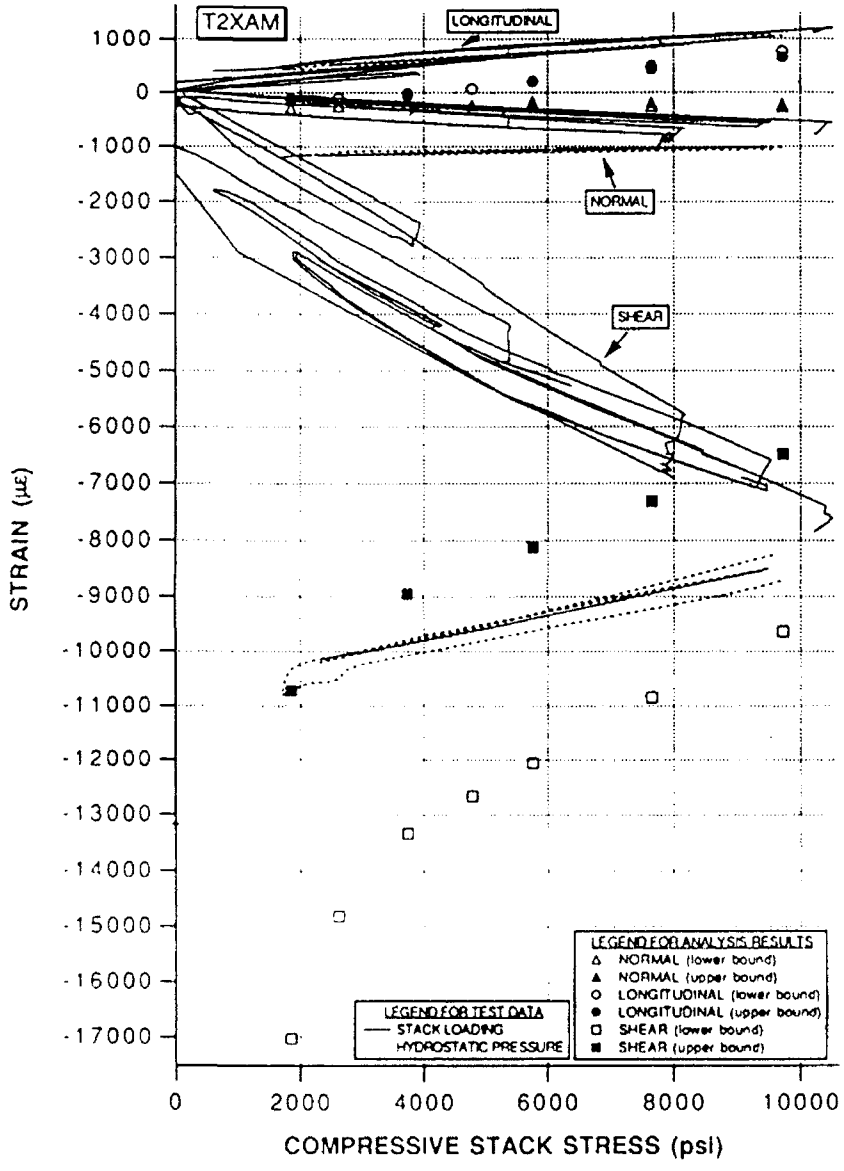

Figure 32 Strain data comparison (Node 1022 versus T2XAM).

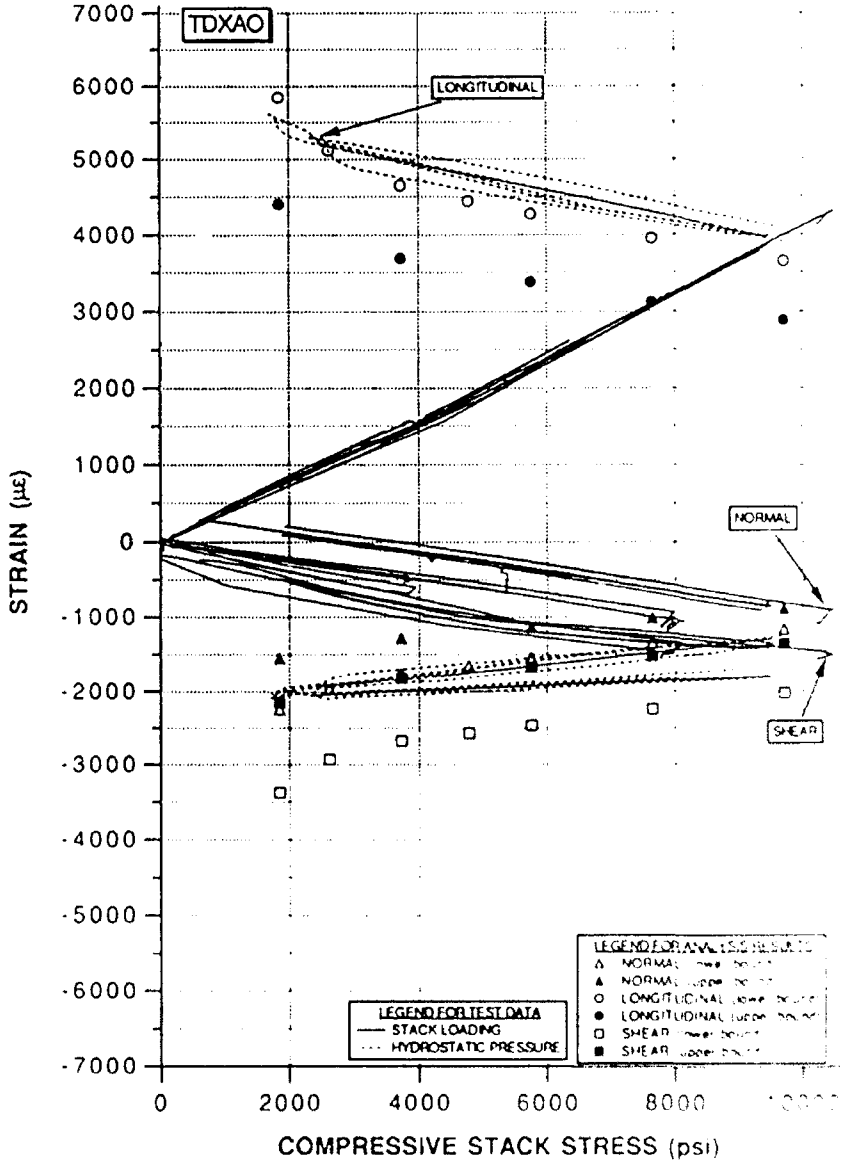

Figure 33. Strain data comparison (Node 1104 versus TDXAO).

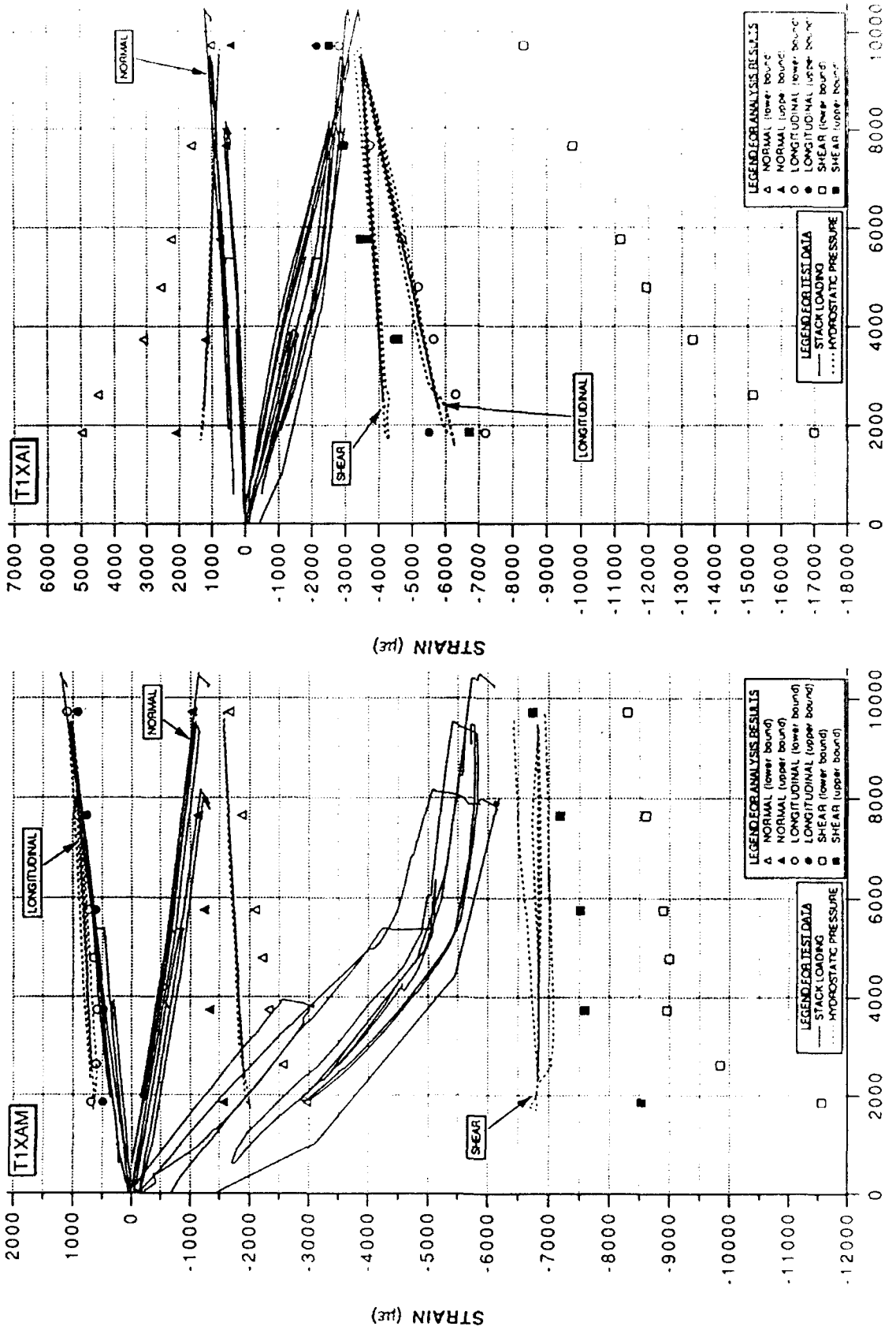

Figure 34. Strain data comparison (Node 1134 versus T1XAM).

Figure 35. Strain data comparison (Node 1115 versus T1XAI).